Separation and Purification Technology 344 (2024) 127247

Contents lists available at ScienceDirect

Separation and Purification Technology

journal homepage: www.elsevier.com/locate/seppur

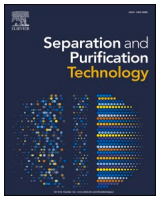

3D printing of a photo-curable hydrogel to engineer mechanically robust porous structure for ion capture or sustained potassium ferrate(*VI*) release for water treatment

Peyman Asghartabar Kashi [a], Adeleh Mohammadi [b], Jianshe Chen [c], Rammile Ettelaie [d], Henry Jäger [e,*], Mahdiyar Shahbazi [e,*]

[a] Faculty of Biosystem, College of Agricultural and Natural Resources Tehran University, Tehran, Iran
[b] Faculty of Food Science and Technology, Gorgan University of Agricultural Sciences and Natural Resources, Gorgan, Iran
[c] Food Oral Processing Laboratory, School of Food Science & Biotechnology, Zhejiang Gongshang University, Hangzhou, China
[d] Food Colloids and Bioprocessing Group, School of Food Science and Nutrition, University of Leeds, Leeds LS2 9JT, UK
[e] Institute of Food Technology, University of Natural Resources and Life Sciences (BOKU), Muthgasse 18, 1190 Vienna, Austria

ARTICLE INFO

Editor: B. Van der Bruggen

Keywords:
UV photocrosslinking
PVA hydrogel
3D printing
Viscoelastic properties
Hierarchical macroporous structure
Adsorption kinetics
Wastewater treatment

ABSTRACT

Contaminated water and scarcity of clean water are becoming progressively serious environmental concerns. Removal of hazardous pollutants from wastewater is vital and urgently needed attention for the protection of pure water resources. To tackle the aforementioned challenges, macroporous structures have great potential to be used in the treatment of heavy metal ions to improve the adsorption efficiency and sustainability of wastewater treatment methodologies. In this context, additive manufacturing technologies have gained considerable attention because of their ability to construct intricate macroporous shapes with multifunctionalities using diverse materials. Here, we used a photocrosslinking graft copolymerization of polyvinyl alcohol/acrylic acid-based ink using UV irradiation in the presence of Norrish type *II* photosensitizer through a hot-melt extrusion-type 3D printer to improve the printing quality of crosslinked ink. The photocured inks offered strong shear-thinning behavior that allowed layer-by-layer deposition to generate well-defined 3D structures, while having sufficiently high viscoelasticity to retain the shape after printing process. With an adequate viscosity at the higher extrusion shearing forces, the 3D printed structures could create multifaceted self-supporting scaffolds with an internal lattice structure that possesses high level of porosity. The hierarchically porous structure of 3D objects showed a recoverable structure yet robust matrix, offering more specific surface area, capable of effectively removing heavy metal ions from water with fast-responsiveness and a high capacity. The ferrate(*VI*)-contained 3D capsule-like object was also detected to be efficient regarding chemical oxygen demand reduction and decolorization of real wastewater. Such 3D-printed hierarchical macroporous objects can offer great prospects in the treatment of water and wastewater purification applications.

1. Introduction

There has been a manifold increase in global wastewater generation over the years because of rapid population growth. The largest part of wastewater discharges involves various effluents made directly into the environment, which then unfavorably influences water quality or causes damage to the aquatic ecosystems and living organisms they contain [1]. More importantly, it has been reported that by 2025 about 1.8 billion people will face water scarcity as a result of global climate change and the lack of efficient wastewater treatment [2,3]. In this regard, there are numerous works nowadays based on reverse osmosis, ion exchange, flocculation-precipitation, and adsorption-based methods focused on implementing effective and ecologically feasible systems to control the evolving concerns of wastewater treatment [4–8]. Among these mentioned methods, the decontamination of aqueous pollutants by adsorptive techniques is the most extensively employed approach owing to their high pollutant removal efficiency, and their economic viability [9].

* Corresponding authors at: Institute of Food Technology, University of Natural Resources and Life Sciences (BOKU), Muthgasse 18, 1190 Vienna, Austria (M. Shahbazi, H. Jäger).
E-mail addresses: henry.jaeger@boku.ac.at (H. Jäger), mahdiyar.shahbazi@boku.ac.at, shahbazim00@yahoo.com (M. Shahbazi).

https://doi.org/10.1016/j.seppur.2024.127247
Received 24 February 2024; Received in revised form 24 March 2024; Accepted 25 March 2024
Available online 29 March 2024

Inspired by natural phenomena, the development of hierarchically porous structures has recently received substantial attention in water treatment, offering fascinating multifunctionality for a variety of challenging applications [10]. To improve the adsorption effectiveness, as well as overcome the drawbacks related to wastewater sustainability, there has been a keen interest in producing hierarchically porous structures with functional materials through innovative approaches [11]. The emergence of additive manufacturing techniques offers a chance to design customized 3D porous structures with controllable macro- and microstructures [12–15]. Three-dimensional (3D) printing, scientifically referred to additive manufacturing, is an innovating assembly layer-by-layer technique, which facilitates the construction of intricate 3D architectures using a bottom–up material accumulation process. This technique can produce a mechanically tunable and high-quality hierarchically porous structure, which allows recycling procedures with a sustainable adsorption rate. As a low-cost, efficient, and versatile technology, 3D printing can also control secondary contamination and simplify the recycling process of adsorbents with no complex treatment processes [16–18]. The utilization of all types of materials, especially biopolymers, paved the way to exploit the effective use of 3D printing in the field of water and wastewater treatments [19–21]. There are different types of 3D printing techniques that are available commercially to produce advanced materials. However, two main methods are commonly applied for wastewater treatment applications, namely extrusion-based [13,22,23] and laser powder bed fusion technologies [24–26]. Several studies have focused on the assembly of 3D printed adsorbents with hierarchical porous structures and on evaluating their potential application to the removal of pollutants from the environment. The reported data from these investigations showed that the 3D-printed adsorbents display outstanding adsorption performances in the rate of adsorption and their adsorption capacity [13,22,23]. For example, Zhou et al [27] used an extrusion 3D printing method to prepare an innovative bionic fish mouth shape adsorbent based on polylactic acid/graphene oxide/chitosan tertiary ink. They reported that this hierarchical porous filter could endow the resulting adsorbent with a cutting-edge ability to efficiently separate a dye from water.

Although the current revolutionary researches can be fascinating, nonetheless their preparation processes contain unsustainable steps including precursor production, solvent evaporation/carbonization, or application of a large number of well-known toxic reagents. Thus, it can be advantageous to design superficial, green, and efficient sustainable materials to prepare hierarchical porous adsorbents for extremely effectual micropollutant elimination. Sustainable adsorbent materials play an important role in water and wastewater treatments, which are obtained from diverse organic and inorganic sources including biomaterial-derived materials [28], clay-based materials [29], and sludge [30]. As a non-toxic and biodegradable material, polyvinyl alcohol (PVA) shows excellent pollutant removal efficiency and reactivity. This is due to its high degree of hydrophilicity, which has been utilized as the matrix of adsorbent for decontamination of aqueous pollutants [31–33]. The PVA-based hydrogel imprinting materials swell in water because of the stretch of the biopolymeric chain structure, where the initial imprinting selectivity can be vanished [34]. The different crosslinking methods have been used to decrease a possible deformation between the biopolymeric chains of PVA in a hydrogel-based system, preserving the imprinted holes principally unaffected [35], and hence upholding the biopolymer selectivity. Yet, the application of PVA-based adsorbents with regard to their structure–function still needs to be much more effective for the removal of contaminants. As mentioned, a macroporous structure is favorably accepted for the dynamic decontamination of inorganic micropollutants from aqueous solution, which can enhance selectivity and efficiency in treating wastewater. Again, crosslinking is the most versatile method for the production of porous hydrogels [11]. By creating a crosslinked network between the polymeric chains, the formation of mechanically robust macroporous materials becomes feasible [12,13].

As a simple, easy-to-operate, and effectual surface modification of biomaterials, the photocuring technique by UV irradiation is extensively utilized to induce crosslinking, commonly operating in the presence of a photosensitizer or photoinitiator. Among the prevailing Norrish type *II* photosensitizer agents, benzophenone [36,37] and its derivatives [38–42] are broadly applied in the polymer crosslinking, which effectively initiates or co-initiates numerous reactive radical species for photocrosslinking. To progress the UV-induced crosslinking, the photoinitiator is decomposed upon irradiation. Subsequently, the reactive radical species are generated and the photocrosslinking process is initiated using a radical mechanism through hydrogen abstraction from the substrate [40].

In the current work, a printable photo-curable hydrogel was produced by UV-irradiation crosslinking graft copolymerization of PVA/acrylic acid, which was 3D printed to produce (*i*) a mechanically robust macroporous 3D adsorbent used to remove inorganic micropollutants and (*ii*) a 3D capsule-like object to encapsulate ferrate(*VI*) for its controlled release in wastewater treatment. In this case, UV irradiation was combined with a Norrish type *II* photosensitizer to synthesize a crosslinked hydrogel-based ink as a precursor for 3D printing process. Thus, sodium benzoate was incorporated into the PVA/acrylic acid system to obtain a photo-curable ink to effectively print a functionalized 3D printed scaffold/capsule-like structure with high absorption ability and recyclability for removal of lead (*II*) (Pb *II*) from aqueous solution. The preparation conditions for the suitability of this ink to fabricate 3D printed scaffolds were investigated by evaluation of different well-defined rheological features, crystalline and thermal properties, as well as through their structural characterizations. The printing performance, microscopic pore structure, and mechanical strength of 3D-printed objects were also assessed. Finally, the sorption mechanisms including sorption isotherms and kinetics were carefully determined.

2. Materials and methods

2.1. Materials

PVA (with an average molecular weight of 72,000 g mol^{-1} and moisture content of 10.2 %) was kindly supplied from Sigma-Aldrich (St. Louis, MO, USA). Sodium benzoate (SB) was provided from Sigma–Aldrich (St Louis, MO). Acrylic acid (AA, anhydrous, Aldrich, 99 % purity, stabilized with 200 ppm of MEHQ inhibitor) was also purchased from Sigma-Aldrich (St. Louis, MO). All other reagents were of analytical grade.

2.2. Preparation of printable ink

The hydrogel-based ink was prepared by dissolving 1 g PVA in deionized water to obtain a concentration of 1 g L^{-1}. Next, the solution was gently stirred at 70 °C for 60 min using a magnetic heater stirrer. To accelerate the dissolution of PVA in water, a high-shear rotor–stator device (SilentCrusher 130 M, Heidolph, Germany) was used, which operated at 24,000 rpm for 5 min. At the same time, AA solution (0.05 g L^{-1}) was incorporated into the prepared PVA-based solution to produce photocrosslinkable ink. Following that, the solution was stirred at 60 °C for a further 60 min to attain a homogeneous mixture.

2.3. Photocrosslinking process

The combination of UV irradiation and SB, acting as a Norrish type *II* photosensitizer, was used to carry out photocrosslinking process. Different concentrations (5–30 wt%) of SB were added to the PVA/AA solution (1 g dL^{-1}), which was then stirred at 60 °C for 80 min. To crosslink the polymer, 20 mL of hydrogel-forming solutions were poured into a specific glass container with a diameter of 7.5 cm, and the solution depth was maintained at 1.5 cm. Next, the photo-curable solution was transferred to a cabinet chamber (this chamber was also in-place

embedded in 3D printer) and exposed to a UV_{254} light source (253.7 nm; 30 W, Kanagawa, Japan) at ambient temperature for 10 min. The light source was 20 cm away from the solution at a 90° angle.

2.4. Infrared spectra measurements

To measure the infrared spectra of crosslinked PVA products, thin films were created and analyzed on a Thermo Electron Corporation Nicolet 6700 Fourier transform infrared (FTIR) spectrometer. To prepare all the samples, 0.03 g of crosslinked PVA products was dissolved in 1 g of di-H_2O at a temperature of 80 °C. The resulting suspension was evenly distributed into three molds, each with a volume of 3.33 mL. These molds were placed in a Teflon sample plate. The samples were then left to dry at room temperature for 48 h. Once the thin films had formed, they were carefully peeled from the Teflon sample plate and further dried in a 90 °C oven for 48 h to remove any possible water trapped in the polymer.

2.5. ^1H NMR measurements

A JEOL's Eclipse$^+$ 400 MHz FT-NMR spectrometer (Japan Electric Co., Ltd.) was used to record ^1H NMR spectra at 70 °C. Before any recording, samples were dissolved in perdeuterated dimethyl sulfoxide (DMSO-d_6, Aldrich) using a 70 °C oil bath. Then, the samples were transferred to 5-mm NMR tubes. The concentration of the sample was 10 mg per 1 mL of DMSO-d_6. An internal standard, tetramethylsilane (TMS), was added to the samples.

2.6. Electron spin resonance

ESR measurements were recorded at a temperature of −196 °C using a Bruker EMX spectrometer (Bruker ELEXSYS E500, Berlin, Germany). This temperature was chosen as there was no significant change in the shape and/or area of the ESR spectra during the analysis (After 48 h of storage at −196 °C, only about 2 % of the total intensity decreased). While the radical concentration decreased significantly in a few minutes at room temperature. Around 20 mg of each ink sample were placed in specialized tubes. The samples were stretched either parallel or perpendicular to the magnetic field axis. ESR spectra were obtained using a 100 kHz magnetic field with 4G modulation, 0.632 mW microwave power, and 9.13 GHz frequency [29].

2.7. X-ray diffraction (XRD) measurement

The XRD pattern was acquired using a Rigaku Ultima *IV* XRD instrument (Tokyo, Japan) The diffraction-angle range covered was from 5° to 50° (2θ), with the diffractometer being fitted with a Cu Kα radiation source (wavelength $\lambda = 1.542$ Å) running at 40 kV and 40 mA.

2.8. Modulated differential scanning calorimetry (MDSC)

The MDSC study was carried out over a temperature span ranging from 3 to 250 °C using a DSC model Q100 that was controlled by a TA 5000 module (TA Instruments, New Castle, DE). The instrument was equipped with a quench-cooling accessory and operated under an N_2 atmosphere at a flow rate of 20 mL min^{-1} with modulated capability. Following the completion of the first scan, the sample was cooled to 3 °C, and a second scan was performed. The total, reversing, and non-reversing signals were distinguished. The crystallinity degree (*CD*) was determined by calculating the enthalpy of melting (ΔH_m) through the integration of the area under the melting peak, using the reference value of $\Delta H_0 = 138.6$ J g^{-1} for 100 % crystalline PVA [55], as illustrated in Eq. (1):

$$CD\ (\%) = (\Delta H_m/\Delta H_0) \times 100 \quad (1)$$

The thermograms were analyzed utilizing the Universal Analysis V1.7F software (TA Instruments).

2.9. Dynamic mechanical analysis (DMA)

The dynamic-mechanical thermal equipment was utilized to conduct DMA assays. This assay involved the use of a clamp tension and a liquid N_2 cooling system. To perform the assays, multi-frequency sweeps were conducted at frequencies of 1, 3, 5, 10, and 15 Hz. The strain amplitude of these sweeps was fixed at 0.1 %. The temperature range for the sweeps spanned from −100 to 200 °C, with a heating rate of 5 °C min^{-1}. Additionally, an isotherm of 15 min at −100 °C was included in the experimental procedure.

2.10. Rheological measurements

The printable inks were tested for their rheological properties using an AR-G2 rheometer (TA Instruments, West Sussex, UK) that had a heating circulator (Julabo, F-12, Seelbach, Germany) attached to it. The samples were placed at the center of the Peltier plate and left for 10 min to reach the equilibrium temperature. The measurements were taken using a rotational rheometer, which was able to measure up to a shear rate of 3000 s^{-1}, and then with a viscometer. When the shear rate exceeded 3000 s^{-1}, the samples were expelled from the geometry in the rotational rheometer. Viscosity measurements were performed using needles with a diameter of 210 μm and a flow rate of 0.25–6 mL min^{-1}. The needles used were 1 in. in length and had a gauge of 27. Many solutions based on PVA display shear-thinning behavior, which means that as the shear rate or stress increases, the apparent viscosity ($\eta = \sigma/\dot{\gamma}$) decreases. Yield stress-type behaviors have also been observed [40]. The Herschel-Bulkley equation (Eq. (2)) was used to describe the relationship between viscosity and shear rate, where τ_0 represents the yield stress, K is the consistency index, and n is the flow behavior index.

$$\tau = \tau_0 + K\dot{\gamma}^n \quad (2)$$

Small-amplitude oscillatory shear (SAOS) experiment was also conducted to determine the linear viscoelastic region (*LVR*) limit. Strain sweep tests were performed at a frequency of 1 Hz to determine the oscillatory shear linear viscoelastic range for each sample separately. Additionally, frequency sweep tests (0.1–100 Hz) were carried out on the inks at a constant shear strain of 1 % ($\gamma = 1.0$ %) within the linear regime. The rheological parameters, including the storage modulus (G') and loss modulus (G''), were obtained from the computer software supplied by the manufacturer (TRIOS, TA Instruments, West Sussex, UK).

2.11. Large amplitude oscillatory shear (LAOS) test

The large amplitude oscillatory shear testing (LAOS) was conducted to study the viscoelastic behavior of samples in the non-linear viscoelastic (*NLVE*) regime. The printing inks were subjected to a logarithmic ramp mode strain amplitude sweep ranging from 1 to 1000 % at a constant frequency of 1 Hz and temperature of 20 °C. The viscoelastic behaviors in *NLVE* were measured as a function of intercycle strain (γ_0), while shear stress (σ) was measured as a function of intracycle strain (γ) and strain rate. Lissajous plots, also known as Lissajous-Bowditch plots, were developed to analyze the non-linear rheological response of inks. This analytical framework was extensively discussed by Ewoldt et al [43]. The differences in the Lissajous plots directly reflect the different *NLVE* properties of inks. The intracycle strain stiffening and intracycle shear thickening behaviors can be evaluated by using an *S*-factor and a *T*-factor, respectively, as defined by Eqs. (3) and (4).

$$S = (G'_L - G'_M)/G'_L \quad (3)$$

$$T = \eta'_L - \eta'_M/\eta'_L \quad (4)$$

Here, $G_L^{'}$ is the large-strain elastic modulus (secant modulus), $G_M^{'}$ is the shear elastic modulus at the minimum strain (tangent modulus at strain zero), $\eta_L^{'}$ is the viscosity at the maximum shear rate, and $\eta_M^{'}$ is the viscosity at the minimum shear rate. Based on the given parameters, when $S = 0$, it indicates linear elastic behavior. On the other hand, when $S > 0$, it means there is intracycle strain stiffening, and when $S < 0$, there is intracycle strain softening. Similarly, $T = 0$ suggests linear viscous behavior, $T > 0$ indicates intracycle shear thickening, and $T < 0$ indicates intracycle shear thinning.

2.12. The 3D printing of hydrogel-based inks

To create 3D-printed objects, the produced inks were printed using an extrusion-based system (nScrypt-3D-450 from nScrypt in Orlando, FL). Before printing, a disposable syringe with a 3 mL volume was filled with the inks. To eliminate air bubbles from the ink suspensions, the syringes were processed with a Vortex mixer (Fisher Scientific, Ontario, Canada) for 4 min. A syringe pump (PHD Ultra; Harvard Apparatus Holliston, MA) was connected to the system to provide a precise extrusion flow rate of 0.40 mL min^{-1}. The printing inks were printed on a plastic surface using a needle diameter of 10 mm and print speed of 15 mm s^{-1} at an ambient temperature.

To create the 3D printed scaffolds or capsule-like objects, AutoCAD software was used to define its shape, and the resulting design was exported in an STL file format (AutoCAD; Autodesk, Cupertino, CA, USA). The G-code files, providing the XYZ pathway instruction of the printer, were then generated by the open-source CAM software Cura™ slicing software (V. 2.3.1., Ultimaker, Geldermalsen, Netherlands) from the STL file. Table 1 lists the settings applied to test the printability and printing the hydrogel-forming inks. Each printed objects had 30 layers. After each layer, the tip's height was raised by 11 mm. The air pressure used for extruding the ink was chosen through experiments and generally ranged from 52 × 105 Pa (22 psi) to 1.72 × 105 Pa (25 psi).

2.13. Characterizations of 3D printed objects

2.13.1. Printing performance of 3D printed objects

Each 3D-printed object was placed in a specific chamber (measuring 20 x 20 x 20 cm^3) to be photographed using a digital camera (Alpha 7 M3 E-Mount, Full-Frame Mirrorless, 24.2 MP, Sony, Tokyo, Japan). The printing accuracy of the 3D-printed structures was determined using a digital caliper (Mitutoyo, Absolute Digimatic, Tokyo, Japan).

2.13.2. Microstructure evaluations of 3D structures

The 3D printed objects were analyzed using a field-emission scanning electron microscope (FE-SEM, S-4700, Hitachi, Japan) to obtain high-resolution images with a greater depth of field. Firstly, each 3D construct was trimmed down to a precise size of (15 × 15 × 15) mm^3. The 3D printed samples were sectioned and then placed on a stage cooled by Peltier technology, which maintained a temperature of −10 °C to prevent thermal damage. Imaging gas nitrous oxide was used at a pressure of 50.7 Pa for capturing the microstructures of each 3D construct. An accelerating voltage of 20 kV was applied to obtain the microstructure images through a solid-state backscatter detector.

Table 1
Printing settings expressed by Cura™ slicing software.

Printing adjusting	Sign	Value	Units	Definition
Nozzle diameter	D	0.3	mm	Nozzle diameter
Layer height	Z	0.1	mm	Layer height
Print Speed	Q	40	mm s^{-1}	Continuous extrusion flow rate provided by the syringe pump
Travel velocity	V_{travel}	80	mm s^{-1}	The spindle speed of a jump between the end of one extrusion and the next
Perimeter	P	2		Number of outline layers
Infill density	ρ_{infill}	100	%	Quantity of material filling the object

2.13.3. Mechanical properties of 3D structures

The tensile stress–strain curves of rectangular 3D printed samples were recorded using a uniaxial tensile tester (Instron 5569; U.K.) with a 10 N load cell at ambient conditions. The experiment was conducted with a constant stretching rate of 50 mm/min. For the experiment, the specimens were cut into a dumbbell shape with dimensions of 35 mm in length, 14 mm in gauge length, 2 mm in width, and 1 mm in thickness. The specimens were stretched at a constant rate of 50 mm min^{-1}. To calculate the nominal tensile stress (σ_M), we divided the force (F) by the initial cross-sectional area (S_0) of the specimens ($\sigma_M = F/S_0$). We defined the tensile strain (ε) as the change in length (ΔL) divided by the original distance (L_0) of the specimens ($\varepsilon = \Delta L/L_0$). We measured the elastic modulus (E) by determining the slope of a linear area (within 5–15 %) of the stress–strain arc. To calculate the toughness (U), we determined the area under the stress–strain plots using the following formula:

$$U = \int_0^{\varepsilon_{max}} \sigma_M d\varepsilon \tag{5}$$

In this experiment, the width of the specimen is represented by W, and the maximum strain experienced by the specimen is denoted by ε_{max}. To obtain the hysteresis area, a successive loading–unloading tensile experiment was conducted. The strain was progressively increased at a rate of 50 mm min^{-1} until failure occurred at a strain of 250 %. The process involved stretching each specimen to the maximum strain of ε_1, followed by unloading it.

The specimen was initially stretched to a certain length and then returned to its original length. It was then reloaded and stretched further to an increased maximum strain (ε_2) at the same velocity rate as the first loading, and then unloaded again. This loading–unloading process was repeated on the same specimen, with the strain increasing each time (ε_3, ε_4, …, ε_n), until the specimen failed at an elongation break. The dissipated energy (U_{hys}) was measured during the loading–unloading cycle using Eq. (6).

$$U_{hys} = \oint \sigma_M d\varepsilon \tag{6}$$

For the tearing test, a trouser-shaped specimen measuring 50 mm in length, 7.5 mm in width, and 1 mm in thickness, with an initial notch of 20 mm, was stretched at a rate of 50 mm min^{-1}. The tearing fracture energy (G) was then calculated using Eq. (7):

$$G = (2F_{ave}/W) \tag{7}$$

The force of peak value upon steady-state tear (F_{ave}) was used along with the specimen width (W) to calculate G. Each experiment was repeated at least three times.

2.14. Adsorption kinetic evaluation of 3D printed objects

The colloidal dispersions containing Pb(II) ions (500 mg L^{-1}) were made using Milli-Q water (100 mL) to assess the adsorption properties of 3D printed scaffolds. In this case, the 3D objects (25 mg) were placed in the colloidal dispersion, which was agitated at a speed of 200 rpm at ambient conditions. An atomic absorption spectrophotometer (AAnalyst400, Perkin Elmer, Norwalk, CT) was used to measure the metal ion contents in the aqueous phase at different contact times (0–60 min). The responses of the spectrophotometer were frequently evaluated with the recognized colloidal dispersion of heavy metal ion standards. Eq. (8) was used to calculate the content of adsorbed Pb(II) ions:

$$q = \frac{(C_0 - C_e)V}{m} \tag{8}$$

In this equation, q (mg g^{-1}) denotes the level of adsorbed Pb(*II*) ions onto a unit mass of 3D printed object; C_e and C_0 represent the levels of Pb (*II*) ions in the aqueous phase after adsorption and in the initial dispersion, respectively (measured in mg L^{-1}). V (L) is the aqueous phase volume, and m (g) specifies the weight of 3D-printed objects [44,45].

To evaluate the adsorption kinetic measurement, the 3D printed structures were exposed to a series of Pb(*II*) colloidal dispersion with varying levels (100 to 600 mg L^{-1}). This experiment was accomplished at given contact times (0–60 min) until an adsorption equilibrium was achieved. Moreover, a similar condition was used to study the impact of pH (2.0–6.0) on the adsorption of Pb(*II*). This measurement was conducted with an initial Pb(*II*) level of 500 mg L^{-1} and an adsorption time of 0–60 min. The hydrochloric acid or sodium hydroxide solution (0.1 mol L^{-1}) was employed to adjust to pH value.

It has been reported that the presence of other types of foreign heavy metal species in wastewater can affect the kinetic adsorption behavior of specific metal ions [45]. For this reason, a study was conducted to analyze the adsorption rate of 3D objects (0.025 g) in the existence of interfering ions such as iron(*III*), chromium(*III*), cobalt(*II*), and Nickel (*II*) with equal concentration (500 mg L^{-1}) at ambient condition.

2.15. Statistical analysis

In the wake of the above-mentioned procedure, measurement analysis of a completely randomized design was carried out with the analysis of variance (ANOVA) followed by Duncan's test procedure in SPSS software (Version 19, SPSS Inc., Chicago, IL). A value of $p \leq 0.05$ was considered statistically significant. The measurements of all the experiments were analyzed in triplicate and the mean and standard deviations of the data were reported.

3. Results and discussion

3.1. Structural and rheological properties of inks

3.1.1. FTIR and ^1H NMR

It has been reported that UV light is unable to direct the rupture of C–C and C–H bonds to form free radicals since it offers only a lower energy level compared to other types of ionizing radiation [46,47]. Henceforth, for photocrosslinking of a polymer, a photoinitiator (photosensitizer) should be added to absorb the low-energy photons (UV irradiation) to be triggered. This can result in the development of free radicals, which cause the macroradical combinations through hydrogen abstraction. The photocrosslinking mechanism by a combination of combination effect of UV light and photosensitizer is not fully explained at present. However, it may include the development of free radicals by photolysis of photosensitizer, which could in turn abstract the tertiary hydrogen atom from the polymeric chains for yielding the polymer macroradicals. This probably crosslinks the PVA polymeric chains by the combination of other such radicals [48].

The preparation of photo-curable hydrogels developed by irradiation crosslinking graft copolymerization of acrylic acid onto PVA was verified by FTIR (Fig. 1a) and ^1H NMR (Fig. 1b) experiments. Fig. 1a illustrates the FTIR spectra of neat PVA-based and photo-curable hydrogels. In the IR spectrum of neat PVA, a wide peak was observed at 3401 cm^{-1} due to the stretching of hydroxyl groups. The typical bands at 2832 and 2794 cm^{-1} were possibly the result of absorptions of asymmetrical and symmetrical stretching of C–H in the polymer's backbone, respectively. The attendance of secondary hydroxyl in-plane bending and C–H wagging vibrations were detected as a result of typical bands of 1453 and 1421 cm^{-1}, respectively [49]. The emergences of typical bands of 1124, 1082, and 985 cm^{-1} were reported for C–C–C stretching and C-O stretching vibration ether C-O-C functionalities, respectively [50].

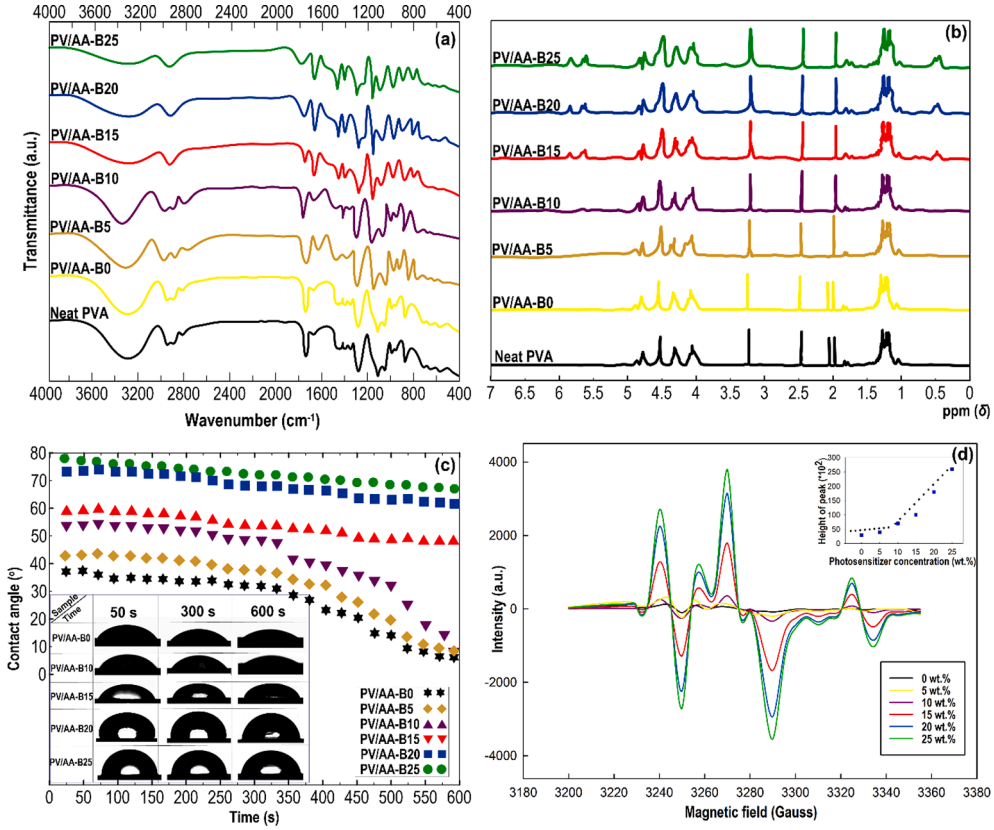

Fig. 1. (a) FTIR, and (b) ^1H NMR spectra of different samples. (c) Dependence of contact angle in time. Inserted images: the image of a water droplet of different samples; (d) Measurement of free radical generations induced by UV-induced irradiation by ESR test.

The FTIR of the PV/AA-B0 (with no photosensitizer) was detected similar to the neat PVA, with neither shift in its typical bands nor the appearance of a new band. Similarly, the characteristic peaks of PV/AA-B5 include the C–H stretching (2832—2794 cm^{-1}); asymmetric stretching vibration of COOH groups (1453 cm^{-1}); CH_2 symmetrical bending (1421 cm^{-1}); and ether C-O-C bands (985 cm^{-1}) were also not changed after photocrosslinking process of PVA. By comparison with the IR spectrum of pristine PVA with PV/AA-B10, the distinctive peaks of OH-stretching (3340 cm^{-1}), C = C (1596 cm^{-1} − 1), and C-O (1461 cm^{-1}) were still present, yet their intensity was reduced and slightly moved to the higher spectrum wavenumbers. The FTIR spectra of PV/AA-B15, PV/AA-B20, and PV/AA-B25, by contrast, showed a notable difference compared to neat PVA, which showed the emergence of two new absorption peaks at 1475 cm^{-1} (C–H) and 1419 cm^{-1} (symmetric −COO– stretching). This specifically revealed the generation of poly (acrylic acid) chains in the hydrogel system. Furthermore, the peak at 1453 and 1421 cm^{-1} in the spectrum of PV/AA-B20 and PV/AA-B25 moved to 1443 cm^{-1} 1406 cm^{-1}, respectively. In the meantime, the band at 1124 cm^{-1} experienced a shift to 1091 cm^{-1}. The band at 1082 cm^{-1} decreased its intensity while the peak at 985 cm^{-1} vanished. The bands at 846, 725, and 680 cm^{-1} also sharpened in the inks with higher SB levels. However, the peaks at 1567 and 1151 cm^{-1} underwent intensity attenuations after photocuring treatment. As can be seen from Fig. 1a, two new peaks appeared at 1790 and 1191 cm^{-1} associated with the attendance of the carboxylic group of the vinyl group.

^{1}H NMR spectroscopy method can also give additional information on the photocrosslinking reaction of the polymeric backbone. The ^{1}H NMR spectra of PVA and its photo-curable products recorded in DMSO-d_6 are shown in Fig. 1b. All signals were effortlessly allocated according to the previous study conducted by Zhang et al [51]. The wide signals centered at about δ 1.25 ppm relate to the methylene protons of PVA. These peaks included both the methylene signals from VOH and vinyl acetate (Vac). It has been reported that about 1 % of VAc is anticipated to be present in the neat PVA [49]. A group of pronounced peaks located at δ 1.95 ppm can be assigned to the methyl group of VAc. According to previous work, an integral value of 200 was utilized for the methylene signals when the integration was 3.1 [49]. These values verified the presence of about 1 % of unhydrolyzed VAc in neat PVA. As can be seen in Fig. 1b, the methyl group peak of VAc (δ 1.95 ppm) remains unchanged for all reactions. Therefore, no reaction occurred among VAc and AA in the presence of SB and UV irradiation. Similarly, no indication of an aldehyde peak is evident in the downfield area of all ^{1}H NMR spectra. The AA molecules should have fully reacted by PVA upon photocrosslinking, which produced a crosslinked network in the ensuing hydrogels. Similarly, PV/AA-B0 showed almost a comparable ^{1}H NMR spectrum in comparison with neat PVA. This shows that introducing AA without photocrosslinking treatment did not affect the molecular structure of PVA, which is in accordance with FTIR result. In contrast, the grafted crosslinking of PVA offered considerable changes in the characteristic peaks of PVA, especially as the NMR signal grew in intensity with increasing SB concentration. In this case, numerous noticeable peaks emerged at δ 0.5–1.80 ppm related to the development of polyacrylic chains [29], a new signal centered at δ 5.6 ppm can be assigned to the acryl group [52], and a signal at δ 5.9 ppm corresponds to protons of the vinyl group [53].

3.1.2. Contact angel

Fig. 1c illustrates the relationship between the contact angle of the grafted hydrogels (their films were prepared by KW-4A spin coater as mentioned in section S-1 in Supplementary Materials) as a function of time, which also included the images of the water droplet change (the inserted images) for 50, 300, and 600 s. Regardless of sample type, the contact angle values of hydrogels reduced gradually in time. It was also observed that PV/AA-B20 and PV/AA-B25 showed lesser dependence on water contact angle from 50 to 600 s as revealed in the inserted images of Fig. 1c. The contact angle data also highlighted that the surface hydrophobicity was enhanced with increasing the level of photosensitizer, which is associated with the development of crosslinked PVA/AA graft copolymer. In this case, the maximum contact angle value of 80° was attained for PV/AA-B25. It is concluded that the graft copolymerized hydrogels have excellent hydrophobicity and stability. This surface improvement is likely because of the presence of a firm structure caused by the development of intra- and interchain interactions in the copolymers.

3.1.3. ESR assay

An ESR was conducted to further detail the molecular level interaction information of the photocrosslinking graft copolymerization of PVA/AA. Fig. 1d shows the free radical development induced by photocuring UV treatment. ESR is a non-destructive technique to analyze the molecular structure and chain dynamics of polymeric materials. The ESR spectra of all hydrogels seemed to include a clear feature at about 3230, 3255, 3270, and 3330 *G*, which is similar to those previously reported for PVA composite [54]. Furthermore, the intensity of ESR signals reveals a noticeable increase with the rising level of SB photosensitizer. Thus, the developed electrons could generate free radicals in the form of unpaired electrons in hydrogels [29]. It could be expected that the free radicals in the adjacent chains are adequately close to each other to make graft crosslinking copolymerization. The peaks of free radicals (at around 3230, 3255, 3270, and 3330 *G*) for control, PV/AA-B0, and PV/AA-B5 were presented with lower intensity if compared with those formed especially in PV/AA-B20 and PV/AA-B25. This indicated that the radicals formed in these hydrogels were successive and continuously reacting.

3.1.4. Kinetics of the crosslinking degree of 3D printed objects

The crosslinking degree of surface grafted hydrogels can be assessed by examining both the surface area normalized swelling rate and hydrogel fraction [29]. The surface area normalized swelling rate (*NSR*) serves as a measure of the density of the newly created crosslinked networks, while the normalized hydrogel fraction (*NHF*) is closely linked to the polymer crosslinking degree [40]. The variations in *NSR*/*NHF* of hydrogels due to UV-induced crosslinking treatment are depicted in Fig. 2a. In essence, as the UV irradiation time increased, the *NSR* decreased and the *NHF* increased for a given SB level. The *NSR* kinetic curve exhibits a plateau shape with a slightly gradual downward slope when the SB was used at the level of < 15 wt%. However, beyond this range, a sharp decline in the curve trend is observed, where the *NSR* was rapidly reduced.

In general, the *NSR* level was higher for control and PV/AA-B0 samples, indicating a greater affinity for water absorption due to the absence of newly formed crosslinked networks. This outcome may lead to an increased rate of adsorption and also enhance the ultimate adsorption capability for Pb(*II*). Upon accomplishment of the treatment, all modified hydrogels presented minimal swelling, signifying a restricted tendency to absorb water. This is likely associated with the reaction between the SB radicals and AA functional groups, leading to the development of intermolecular linkages between PVA chains. In contrast, PV/AA-B20 and PV/AA-B25 demonstrated resistance to water swelling as a result of graft crosslinking copolymerization, resulting in a limited ability to absorb water. This behavior is linked to the development of an intermolecular network involving PVA, AA, and SB upon UV irradiation. The data presented in Fig. 2a illustrates that PV/AA-B5 exhibited the highest *NSR* of 5.12 cm^{-2}, followed by PV/AA-B10 with an *NSR* of 5.04 cm^{-2}. However, PV/AA-B20 and PV/AA-B25 showed a sharply downward slope of *NSR* with a value of 2.90 and 1.1 cm^{-2}, respectively, which is due to the formation of a significant amount of chain crosslinking/branching. This shift indicated a lower tendency for water absorption due to formation of structured networks.

3.1.5. XRD patterns

Fig. 2b illustrates the crystalline properties of neat PVA and various

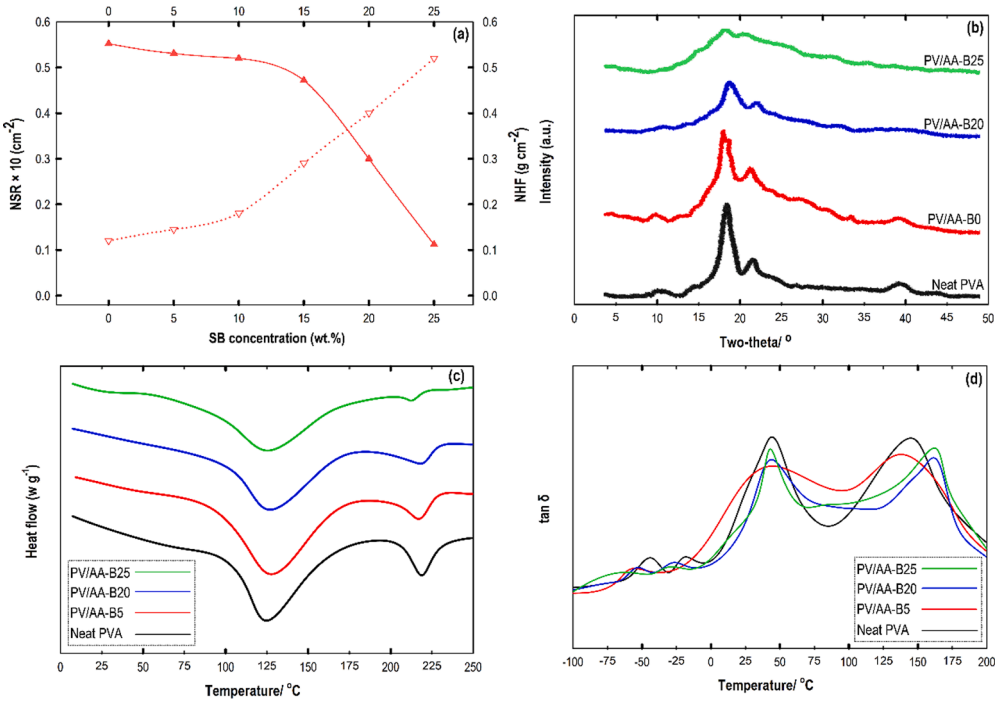

Fig. 2. (a): Changes in normalized swelling rate (solid symbols) and normalized hydrogel fraction (hollow symbols), (b): XRD patterns, (c): DSC thermograms, and (d): DMA spectra of different samples.

modified PVA/AA hydrogels. The distinct peaks of neat PVA were detected at $2\theta = 10.9°$, $18.9°$, $23.1°$, and $39.9°$. Conversely, the diffraction pattern of PAA did not exhibit any peaks (its diffractogram was not shown), proposing an almost amorphous nature. In the presence of AA monomer and SB, a slight reduction of the hydrogel crystallinity was noted as the SB content was increased (Fig. S-1, section S-2, in Supplementary Materials). Specifically, the main peak of $2\theta = 19.7°$ was still evident in the diffractogram of these grafted samples, which shows the crosslinking graft copolymerization was performed in the semi-crystalline area. On the other hand, the intensity of the main peak regarding PV/AA-B20 and PV/AA-B25 decreased, and the characteristic peaks located at $2\theta = 11.4°$ and $41°$ disappeared (Fig. 2b), which can be associated with an effective reduction in the crystallinity of these 3D printed structures. This outcome results in the disruption of hydrogen linkages between the hydroxyl groups of PVA because of interactions with carboxyl groups of AA, in addition to the development of PAA and its grafting onto the hydrogel network. Preceding works also reported comparable deformations in crystal structures of PVA-based hydrogel [31,32].

3.1.6. Thermal properties

Fig. 2c displays the DSC thermograms of PVA and various PVA/AA hydrogels after graft crosslinking copolymerization. There are two endothermic peaks in the thermogram of neat PVA and PV/AA-B0 (not shown); the first transition is likely associated with the evaporation of water from the polymeric system, whereas the second peak at about 218 °C showed the melting of the crystalline domains. The crystallinity degree of PVA was measured by Eq. (1), where it was detected to be comparable to that of the X-ray experiment (data not shown). The results were also consistent with the findings of Hasimi et al [55]. Similar to neat PVA, PV/AA-B5 also possessed two endothermic events, though the enthalpy of the first peak increased by about 17 % in comparison with the neat PVA. This is likely because of a greater moisture content caused by AA incorporation. However, the enthalpy of the second transition assigned to the melting of the crystalline region became less prominent, offering a decrease of about 27 %. The enthalpy reduction of the melting peak presents a reduction in the crystallinity and perfection of the crystal structure in the hydrogel network. This outcome is possibly related to the interaction between PVA and AA in the amorphous domain, leading to the crystal disordering with a decrease in the enthalpy of the phase change. A comparable behavior was detected in PV/AA-B20 and PV/AA-B25. It is anticipated that the degree of the amorphous domains in the crosslinked samples was increased, while the crystallinity degree experienced a notable decrease. These results were supported by XRD analysis (Fig. 2b). Following the UV treatment, a notable alteration occurred in the arrangement of the polymer chains within the network, leading to a considerable displacement of both endothermic occurrences towards the lower temperatures [56]. It has been revealed that the amorphous region would be only susceptible to the chemical and free radical attack, which encompassed variations in the crystallite thickness and crystallinity degree [40].

3.1.7. Dynamic mechanical analysis (DMA)

Concerning DMA analysis, two typical signals (labeled as β and α) were recognized in the DMA spectra of all samples with increasing temperature (Fig. 2d). The β relaxations, detected at about -50 and -25 °C, were related to the water relaxation, assigned to the hydroxyl motions induced by water molecules [57]. The peak temperature corresponding to the β relaxations was reduced after graft crosslinking copolymerization. Moreover, the tan δ curves of the DMA spectra showed that the intensity of these relaxations reduced, which was possibly associated with a trivial limitation of side chain movements because of the grafting of AA or an increase in density resulting from the development of a crosslinked network.

The DMA analysis also showed that the second typical relaxation represented as α peak, which was also a lower intensity in the crosslinked samples. The temperature at which the α relaxation occurred is defined as the dynamic glass-transition temperature (T_g), which is a sign of system miscibility [48]. The presence of two distinct T_g behaviors proposes a moderately miscible system. The detection of two relaxation peaks signifies the presence of a heterogeneous two-phase structure in the materials. While it can be possible to differentiate between a miscible system and a phase-separated one through DSC if their T_g differs by more than 20 °C. However, this distinction was not achieved in

the current work except through DMA analysis. The DMA curves of crosslinked hydrogels displayed two primary thermal events at increasing temperatures, closely corresponding to the T_g of the PVA-enriched phase and the developed grafted poly(acrylic acid)-enriched phase (Fig. 2d). To elucidate these phenomena, the complexity of the study system must be taken into consideration. As noted by Krumova et al [57], PVA is a semicrystalline polymer characterized by physical interactions between polymeric chains resulting from hydrogen bonding among hydroxyl groups. Consequently, the formation of graft crosslinking copolymerization led to changes in both the physical network and crystallinity of the system, resulting in variations in the T_g values. The change in the T_g of the components indicates a level of miscibility between the homopolymers due to interactions between the polymers. Moreover, the shift in transition temperatures across the temperature range suggests incomplete phase separation and the presence of an interphase. The T_g of the PVA-enriched phase was observed at the lower temperatures compared to other samples. This change indicates that the alteration in the matrix composition resulting from the graft crosslinking copolymerization had a greater impact on the PVA-enriched phase.

3.1.8. Flow behavior

The printability of polymers-based inks is an important factor in developing a high-performance 3D structure, which can be strongly affected by the flow behavior of the inks. Definitely, the ability of inks to squeeze from the nozzle of a printer is related to their rheological properties such as apparent viscosity, flow behavior index, and yield stress. The PVA-based hydrogels have been reported to prove shear-thinning behavior and yield above a threshold level of crosslinking moiety. The development of crosslinking graft copolymerization produces a structure, which should yield before flow starts [58]. Regarding hydrogels exhibiting a yield phenomenon, a gel-like response occurs at stresses below the apparent yield stress for which the material will not flow. The material begins to flow once the yield stress is exceeded [59]. Since crosslinked PVA-based hydrogels often possess yield stress, experimental measurements were conducted with induced shear stress to obtain pre-yield and yielding responses [60]. To detect the flow behavior of the hydrogels, a steady-state controlled shear stress sweep ranging from 0.1 to 100 Pa (Fig. 3a), followed by an imposed shear rate sweep from 0.1 to 1000 s^{-1} (Fig. 3b), was applied. Fig. 3a illustrates apparent viscosity as a function of shear stress, where a yielding behavior was obviously detected for PV/AA-B25 since the viscosity values dramatically reduced by several orders of magnitude for a small increase in stress. For PV/AA-B20 a sharp decrease in viscosity was also observed after 10 Pa. The plots of apparent viscosity against shear stress for a polymeric system typically contains three main areas; a high viscosity Newtonian-like plateau at a low shear stress, followed by a shear-thinning regime (representing structural breakdown), and eventually an additional Newtonian-like part at the higher shear stresses [61], where the aggregated structure is fully broken down and thus cannot alter any further. As expected, control (neat PVA) with no crosslinking treatment showed a weak structure, in which a continuous flow curve with no yield stress was detected. Similarly, PV/AA-B0 viscosity slowly drops with increasing shear stress with no yield stress, showing a weak structure and rapid failure upon the application of shear stress, even at relatively low values.

A viscosity experiment was carried out across five orders of magnitude (Fig. 3b) to monitor the flow properties of inks at rest and upon the extrusion shearing forces anticipated during 3D printing through small diameters of needles. As illustrated in Fig. 3b, a viscometer is often an endorsed technique to measure the flow behavior of polymer-based inks at a high shear rate, removing the requirement of *ad hoc* correction in addition to test challenges during rotational rheometer [62]. Fig. 3b

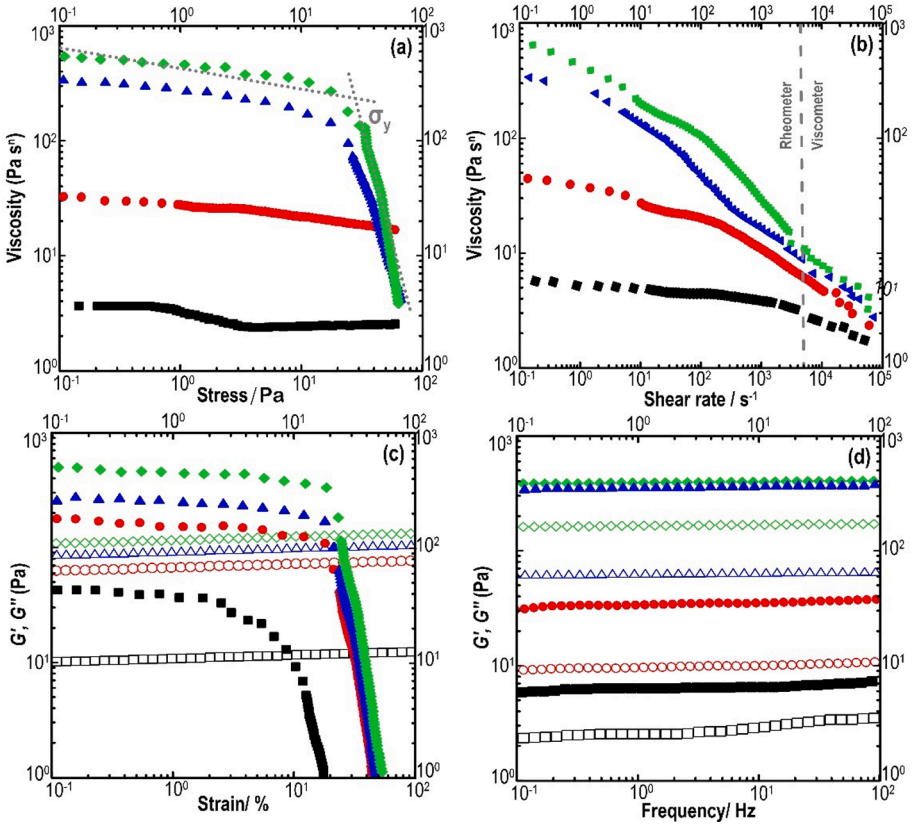

Fig. 3. (a) Viscosity versus stress to highlight the yield stress and transition to a flow regime and (b) Viscosity versus shear rate showing drastic shear-thinning behavior (σ_y denotes extensional or uniaxial yield stress). (c) Oscillatory strain sweep plots, where G' is solid symbols and G'' is open symbols; and (d) Oscillatory frequency sweep. The results are shown for control (■), PV/AA-B0 (●), PV/AA-B20 (▲), and PV/AA-B25 (◆).

clearly shows the graft crosslinking copolymerization dramatically increased the apparent viscosity at shear rates up to 100 s^{-1}. However, the differences between the viscosity values of the control and the crosslinked samples went to zero with an increasing shear rate. In this case, the viscosity values of the crosslinked inks approached those of non-crosslinked samples.

Table 2 shows the flow behavior parameters including flow behavior index (n) and consistency index (K) in the high or low shear rates, which were determined by fitting the flow portion (post-yield) of viscosity versus shear rate data to a Herschel-Bulkley model (Eq. 2). The fit was performed in the low shear rate range 1–100 s^{-1} and the high shear rate range between 10^3-10^5 s^{-1}. The low shear rate range is the most commonly reported for physically associated hydrogels, while the high shear rate range is the operative range for the 3D printing process at clinically relevant flow rates [60,61]. The shear-thinning process is highly nonlinear and can be observed through a non-sinusoidal response when subjected to sinusoidal applied shear. The shear-thinning parameter ranges from 0 to 1, where 1 corresponds to a Newtonian (shear rate-independent) viscosity. Some of the physical hydrogels exhibit both viscous flows under shear stress (shear-thinning) and time-dependent recovery upon relaxation (self-healing), providing an alternative strategy for printing hydrogel applications.

The Herschel-Bulkley response obtained at the low shear rates (1–100 s^{-1}) was completely different compared to the Herschel-Bulkley response obtained at high shear rates of 10^3-10^5 s^{-1}. The polymeric-based inks showed more shear-thinning behavior at a higher shear rate region ($\dot{\gamma} > 10^3$ s^{-1}) than that in the low shear rate region (1 s^{-1} < $\dot{\gamma}$ < 100 s^{-1}). In this case, PV/AA-B20 and PV/AA-B25 confirmed tremendously higher shear-thinning properties ($n < 0.5$) at higher shear rates. It can be hypothesized that improving shear-thinning behaviors at high shear rates is due to further breakup of remnant structures as a result of the development of inter- and intramolecular interactions inside the crosslinked hydrogels. This leads to a very broad yielding transition before simple shear-thinning is observed. It has been stated that with increasing the number of physical interactions of polymers, a comparatively wide yielding transition was detected, whereas a sharp yielding transition was noticed for crosslinked systems [60,63].

3.1.9. Small-amplitude oscillatory shear (SAOS)

The SAOS measurement is often used to characterize the linear viscoelastic properties, where the relation between applied stress and induced shear is assumed to be linear. To determine the limit of the linear viscoelastic region (*LVR*), a strain sweep test was initially conducted (0.01–100 %, 1.0 Hz). Fig. 3c shows storage (G') and loss (G'') moduli as a function of strain sweep. At the low strain values (<1%), within *LVR*, the strain amplitude possessed a little impact on the $G'(\gamma)$ and $G''(\gamma)$, and always $G'(\gamma) > G''(\gamma)$ regarding all samples. This implied that the hydrogel-based inks offered an elastic stable structure. The viscoelastic moduli of the samples (excluding control) fairly persevered in the *LVR* up to a strain of around 10 % with a slightly decreasing trend in the $G'(\gamma)$ values, followed by an important decrease in the $G'(\gamma)$ values for strains exceedingly around 30 %. The viscoelastic moduli of the hydrogels were detected to be dependent on the level of SB photosensitizer. Overall, the $G'(\gamma)$ of PV/AA-B0 was slightly higher than the control sample, followed by PV/AA-B20. The PV/AA-B25 showed the highest $G'(\gamma)$ values, highlighting the development of a strong structured gel-like system.

The mechanical property of the hydrogels was further assessed as a function of oscillation frequency sweep test. Concerning all the materials that formed crosslinked structures, the $G'(\omega)$ exceeded the $G''(\omega)$, which is indicative of elastic or gel-like behavior of the systems (Fig. 3d). From the frequency sweep, it is observed that the mechanical features of the hydrogels were comparatively independent of the oscillation frequency. As shown in Fig. 3d, all hydrogels presented steadily higher $G'(\omega)$ values than those of $G''(\omega)$ in the whole frequency range. This specifies that the hydrogels were quasi-solid behavior, offering a more structured and connected network. Also, the extent of $G'(\omega)$ values was particularly increased with increasing the level of photosensitizer. This rationally emphasizes the development of a strong polymeric gel-like network, which may be due to the formation of more intra- and inter-chain interactions within the copolymers. Therefore, the resulting strong gel-lie viscoelastic structure, obtained by higher photosensitizer levels, can be advantageous for processing in 3D printing. This helps the printed objects endure their shapes following the application of shearing forces during 3D printing. This consequently enhances the printability and printing accuracy of 3D-printed objects.

3.1.10. Large-amplitude oscillatory shear (LAOS)

Complex polymeric systems with comparable linear viscoelastic behaviors display dissimilar nonlinear viscoelastic properties [64]. In this case, viscoelastic moduli are detected according only to a first harmonic contribution to a stress response, which as a result is likely to possess a somewhat vague physical meaning in the sense that in the non-linear viscoelastic regime, many harmonics will also be present due to the non-linearity. Hence, a LAOS measurement, which provides a more accurate way of dealing with the non-linear viscoelastic behavior through providing elastic or viscous Lissajous plots, was accomplished to detect the complete oscillatory response at each imposed intracycle strain (γ_0) (Fig. 4). The normalized Lissajous plots of shear stress (σ) as a function of γ are shown in Fig. 4, Left, denoted as 'elastic' Lissajous plots. The enclosed area of the 'elastic' Lissajous plot is associated with the dissipated energy (proportional to G''), which the decomposed elastic stress (σ_e) in the inner loop shows the purely elastic contribution to total shear stress (σ). The 'elastic' Lissajous plots of all samples displayed an elliptical narrow shape once γ_0 was equal to 6.34 %. The σ_e was a straight line, which is characteristic of *LVR* property. The PV/AA-B20 and PV/AA-B25 offered noteworthy narrower ellipses, denoting a lower dissipated energy per cycle compared to other samples, indicating the dominance of elastic behavior over viscous ones. This agrees well with the SAOS data about substantially higher G' values of these samples (Fig. 3c,d).

As can be seen in Fig. 4, Left, the Lissajous plot of PV/AA-B20 and PV/AA-B25 remained narrow with an almost elliptical shape as γ_0 increased to 25.2 %. Inversely, the Lissajous plots of control and PV/AA-B0 became distorted, showing the effect of higher harmonics. This highlighted the fact that these two samples are well into the non-linear viscoelastic region while PV/AA-B20 and PV/AA-B25 were still in the *LVR* at this strain. In this case, the distortion of Lissajous plots was diverse in magnitude, varying with the type of sample. Regarding PV/AA-B20, its Lissajous plot only offered a minor upswing, representing a slight intracycle strain stiffening impact. The alterations among the loop of σ and σ_e remained not very significant. Concerning control and PV/AA-B0, their Lissajous plots were altered to a parallelogram-like form, where the surrounding area was prolonged notably, indicating a

Table 2
Herschel-Bulkley fits for different hydrogels. The shear-thinning parameters include K (consistency index (Pa s^n) and n (flow behavior index). Herschel-Bulkley for shear rate in the range of 1–100 s^{-1} ($\dot{\gamma}_{Low}$) and 5 × 10^3 to 300 × 10^3 s^{-1} ($\dot{\gamma}_{High}$).

Sample	$\dot{\gamma}_{Low}$			$\dot{\gamma}_{High}$		
	Yield stress (Pa)	***K* (Pa s^n)**	**N**	***Yield stress (Pa)***	***K* (Pa s^n)**	***n***
Control	0.88 ± 0.02^b	0.96 ± 0.02^b	0.87 ± 0.001^c	0.45 ± 0.01^a	0.49 ± 0.02^b	0.82 ± 0.001^d
PV/AA-B0	0.72 ± 0.01^a	0.85 ± 0.01^a	0.70 ± 0.003^a	0.44 ± 0.01^a	0.41 ± 0.01^a	0.71 ± 0.002^c
PV/AA-B20	8.44 ± 0.07^c	33.81 ± 0.64^c	0.68 ± 0.002^b	8.12 ± 0.05^b	20.7 ± 0.64^c	0.49 ± 0.001^b
PV/AA-B25	9.92 ± 0.06^d	124.37 ± 1.03^d	0.60 ± 0.001^a	9.56 ± 0.04^c	96.66 ± 1.03^d	0.42 ± 0.002^a

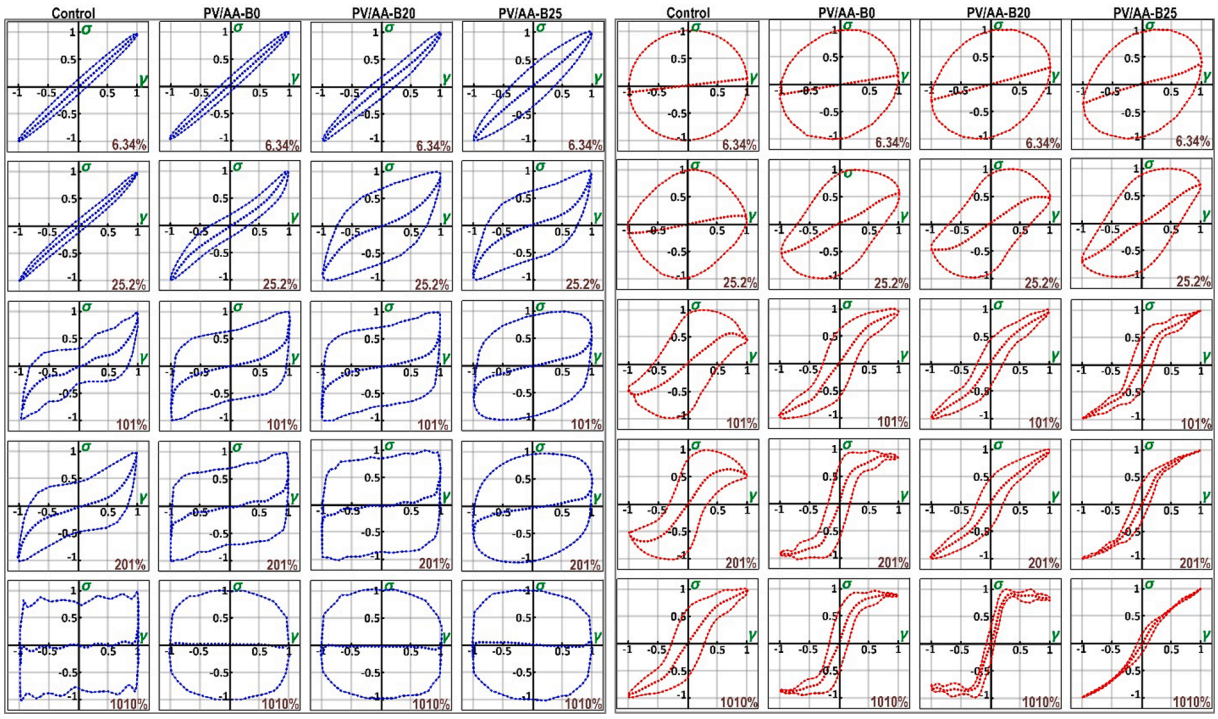

Fig. 4. Area surrounded by the "elastic" (Left) and "viscus" (Right) Lissajous-Bowditch plots as a function of amplitude (a frequency of 1 rad s^{-1}). Stress and strain results are normalized with a maximum stress/strain in the oscillation cycle.

significant breakdown of network structure. With increasing γ_0 to 101 %, a different upswing behavior can be detected in the total stress concerning PV/AA-B20 and PV/AA-B25, where there was also a considerable structural breakdown related to the stretching of residual structure. For control and even PV/AA-B0, this upswing was apparent only in the elastic contribution with approaching the extreme intracycle strain. In addition, their Lissajous plots have already altered to a square-like form with no additional change even when γ_0 further enlarged. This implies a decline in the elastic behavior of the control and PV/AA-B0.

In the case of γ_0 equal to 201 %, a parallelogram-like shape was observed in the Lissajous plots for all the samples. Now all samples are well beyond their linear viscoelastic limit. There might be an intracycle sequence of elastic straining (the vertical part), yielding, flow (the nearly horizontal part), and (partial) recovery for PV/AA-B25, PV/AA-B20, PV/AA-B0, and control, respectively. In this case, the Lissajous plot of PV/AA-B25 presented a smaller surrounding area compared to PV/AA-B20. Additionally, these samples also displayed a narrower Lissajous plot compared to PV/AA-B0 and control. These outcomes point to the fact that the higher levels of photosensitizer contributed to a hydrogel with a moderately stronger elastic property. At the maximum tested γ_0 of 1010 %, the Lissajous plot of all samples was changed to an almost rectangular-like geometry, representing their behavior from a principally elastic form to nearly perfect plastic property [43]. For PV/AA-B0 and control, the Lissajous plots endowed straighter and sharper corners, demonstrating a more sudden intracycle-yielding behavior. Alternatively, Lissajous plots of PV/AA-B20 and PV/AA-B25 exposed more round and smoother corners, presenting a steadier yielding property.

The normalized 'viscous' Lissajous plots of σ versus intracycle strain rate ($\dot{\gamma}$) are also shown in Fig. 4, Right. Compared to the 'elastic' Lissajous plots, the surrounding zones of 'viscous' Lissajous plots are associated with the stored energy (related to G'), and the dashed lines within the middle specify the contribution of a viscous stress (σ_v) to σ. All samples showed spherical curves regarding σ, but straight lines for σ_v once γ_0 was 6.34 %. This is according to the mainly elastic behavior in the *LVR*. With increasing γ_0, the surrounded part of the 'viscous' Lissajous plots reduced in the order of control < PV/AA-B0 < PV/AA-B20 < PV/AA-B25. In the meantime, 'viscous' Lissajous plots of all samples possessed a sigmoid-like shape beyond γ_0 of 101 %. This reveals the presence of an intracycle shear-thinning property because of the disruption of the structural network of hydrogels and the arrangement of segments in the direction of the flow. At the largest γ_0 (1010 %), a secondary loop was clearly detected in the 'viscous' Lissajous plots of PV/AA-B20. This specific geometry can be an indicator of overshoot in the stress, which is likely related to a strain overshoot (Type *III* and Type *IV*) LAOS behavior. One conceivable explanation for the observed stress overshoot can be a link between the elasticity of the sample with instrument inertia [65]. Such a phenomenon also appears once the time scales of the rearrangement of the microstructures are shorter compared to that of the deformation [43]. In the current study, an uneven secondary oscillation (wave-like horizontal portion) was detected in the 'elastic' Lissajous plot at a strain of 1010 % (Fig. 4a), which causes us to believe that elasticity-inertia linking is likely.

3.2. Characterization of 3D printed samples

3.2.1. Scaffold morphology

The microstructures of the 3D printed scaffolds were evaluated by SEM (Fig. 5). The 1D filament printed by control and PV/AA-B0 inks possessed an irregular geometry with a diameter of about 538 and 523 μm, respectively. Similarly, the cross-section of the fracture surface of 1D filament produced by control and PV/AA-B0 inks was rough with several irregularities on the surfaces. Inversely, PV/AA-B20 and PV/AA-B25 inks offered an even 1D filament with a diameter of about 520 and 512 μm, respectively. In addition, the rupture surface of the 1D filament for these samples was smooth and circular, which could lay the basis for the printing of superior more intricate objects. Similarly, the self-supporting scaffold (pore size with a 0——90° log-pile structure) for PV/AA-B20 and PV/AA-B25 showed well open porosity that was geometrically ordered and interconnected. The control and PV/AA-B0 again showed a shape deformation with curve-like angles, suggesting dimensional instability. This also led to some levels of extension of the

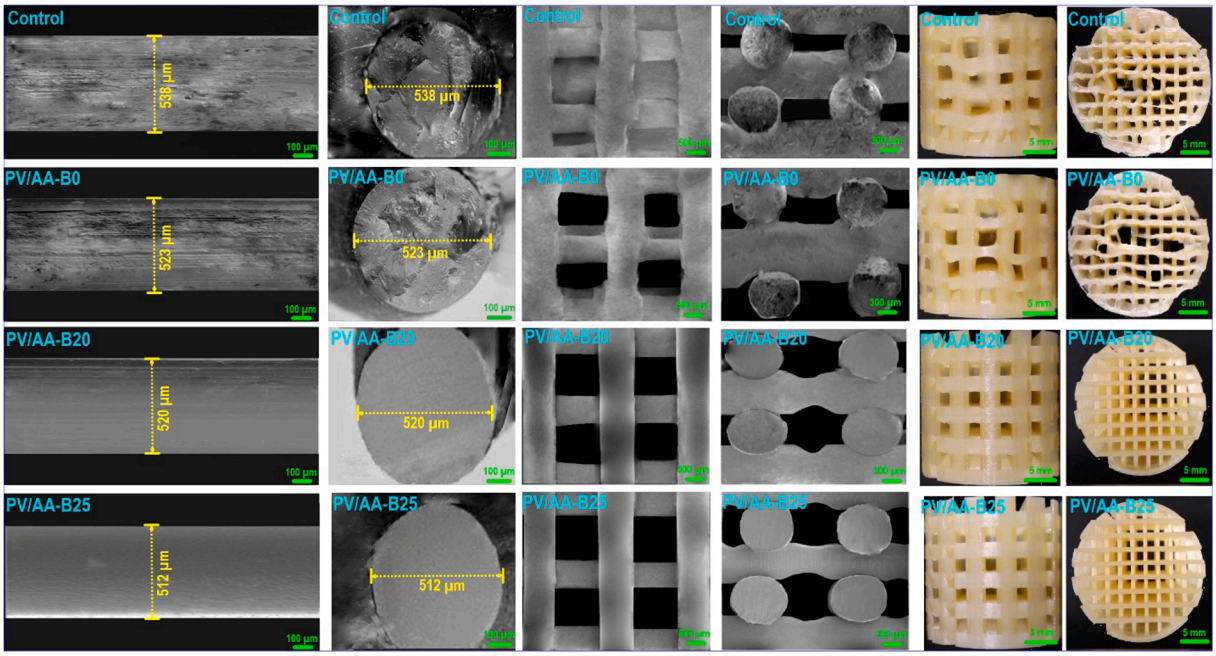

Fig. 5. SEM images of 3D-printed grids as well as their relevant photomicrographs of the surface or cross-sectional rupture of different 3D printed filaments. From Left-to-Right: FE-SEM images of the surface of 1D printed filaments (first column), their relevant cross-section raptures (second column), 0 – 90° log-pile structure (third column), cross-section of log-pile structures (fourth column), and printing quality images of 3D printed objects (fifth and sixth columns).

line-edge roughness compared to a 3D structure printed with PV/AA-B20 and PV/AA-B25 inks. As mentioned earlier, the development of a gel-like structure in the latter samples could describe this difference in the precise geometry and shape fidelity.

Fig. 5 also illustrates the optical images of the printed objects. The morphology of 3D printed PV/AA-B20 and PV/AA-B25 scaffolds showed higher printing performance with a precise geometry and enhanced shape fidelity. They displayed an open porous geometrically ordered and interconnected structure. In this case, an improved elastic modulus (Fig. 3d) with a higher degree of nonlinear behavior (Fig. 4) were achieved by increasing the level of photosensitizer. This led to better spatial resolution and 3D printing performance. The printed structures based on control and PV/AA-B0 scaffolds, by contrast, had irregular geometries and the printed parts and pores between them are clearly seen to be nonuniform, presenting an inferior printing quality and poor dimensional stability.

As an effective 3D material for water adsorption, a sponge-like structure with a hierarchically macroporous architecture possesses the advantages of lightweight, high porosity, large surface area, high water adsorption rate, and easy construction [66]. Thus, using these structures as self-contained adsorbents can serve as a perfect choice for water treatment applications [67]. To design customized 3D porous structures with controllable macro- and microstructures, a freeze-drying method was used for the prepared 3D printed structures, which can allow for discrete control of spherical pore diameter to yield a hierarchical macroporous structure. In this case, a 3D-printed capsule-like object with several visible pores was produced followed by a freeze-drying technique (Fig. 6). This technique can control the interconnections between macropores to allow for mass transport or water absorption throughout the constructs. The printing quality images of whole printed parts of freeze-dried printed PV/AA-B20 and PV/AA-B25 confirmed a good shape retention with no structural deformation and sagging along the *z* direction. In contrast, control and PV/AA-B0 showed a poor shape-fidelity with a random and missing distrusted visible pore size due to a weak structure. The representative FE-SEM images of all freeze-dried printed capsule-like objects are also provided in Fig. 6. By analysis of FE-SEM images, the microstructure of control was characterized to be a compact structure with some irregularity and no apparent pore structure within the matrix. Similarly, PV/AA-B0 seemed to be notably uneven, also having an uneven microstructure. Remarkably, printed PV/AA-B20 and PV/AA-B25 showed a 3D interconnected porous structure with blurry sieve-like ones and several aperture diameters in nanometers size, having a pore size varying from about 80 to 600 nm. Compared to PV/AA-B20, PV/AA-B25 presented a more randomly opened macroporous structure within an interconnected matrix possessing thicker pore walls, having more specific surface area (Table S-1, section S-3, in Supplementary Materials). The resultant thick pore wall can endow a more supporting capacity, and therefore may lead to enhanced captivating adsorption effectiveness. Thus, this meets the requirement for potential application in water purification.

3.2.2. *Mechanical strength and self-recovery of 3D printed objects*

The typical tensile stress–strain plot with its relevant stress bar chart for different 3D printed samples is shown in Fig. 7. The stress–strain plots clearly revealed that the graft crosslinking copolymerization remarkably affected the mechanical strength of printed objects. The PV/AA-B20 and PV/AA-B25 offered a greater elastic modulus (*E*) (Fig. 7a) with higher fracture energy (*G*) (Fig. 7b) in comparison with control and PV/AA-B0. This outstanding mechanical property can be a result of the enhanced crosslinking density of the 3D network owing to the development of intermolecular bonds.

Fig. 7c also illustrates the recovery features of printed samples evaluated by loading–unloading measurement at a 250 % strain. According to the obtained results, an unimportant hysteresis loop was detected for control, which endowed unrecoverable deformation during the unloading process. This shows the attendance of a huge effective energy dissipation pathway within its specific network matrix. Similarly, PV/AA-B0 offered a characteristic unrecoverable deformation, which remained slightly unaffected during load–unload cycle. This revealed the lack of softening during the loading–unloading process, denoting an unrecoverable deformation with a low level of toughness (Fig. 7d). Inversely, 3D printed PV/AA-B20 and PV/AA-B25 objects endowed a larger hysteresis loop, therefore attaining maximum toughness with high self-recovery properties. This proposes that they

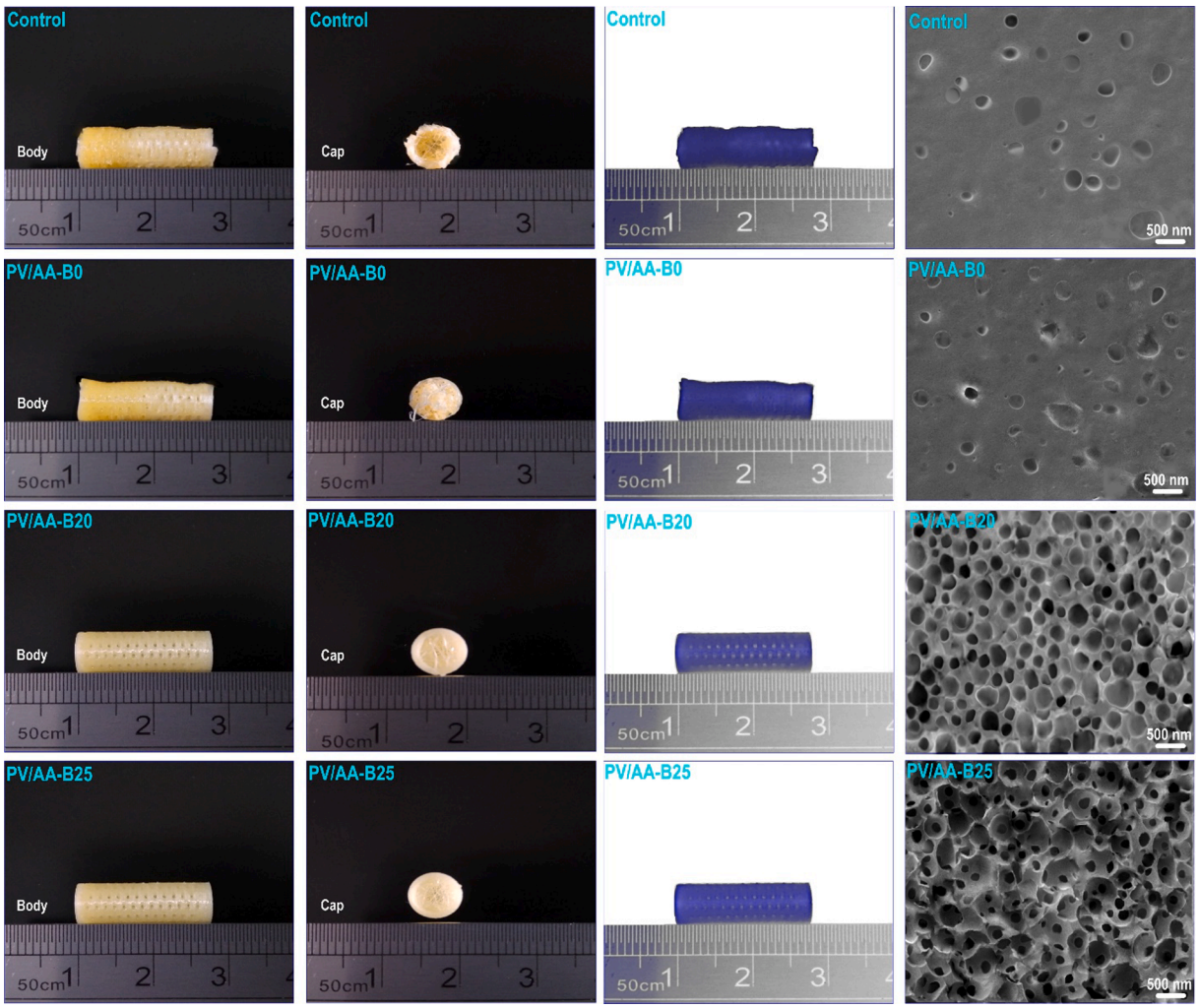

Fig. 6. The printing performance comparison of different 3D printed objects in relation to their FE-SEM images.

possessed a typical rubber elastic feature with regards to low-amplitude deformation, yet they offer excellent mechanical self-recovery behavior at a high-amplitude deformation. This is possibly elucidated by an interconnected crosslinked network in 3D printed structures.

3.3. Adsorption kinetics of multifunctional 3D printed objects

3.3.1. Impact of contact time

Contact time shows the adsorption kinetic of an adsorbent for a given initial adsorbate amount, which is a critical parameter to monitor the adsorption capacity of adsorbents [29]. The adsorption rate of 3D capsule-like objects on Pb(*II*) ions in time is shown in Fig. 8a. With increasing time, the ion removal capacity of 3D capsule-like objects was increased in all samples. At the initial contact time (lower than 10 min), all 3D constructs showed a maximum Pb(*II*) adsorption capacity, followed by a plateau region (denoting adsorption equilibrium). This adsorption behavior has been reported in other classes of adsorbent materials [44,45,68]. In the adsorption equilibrium level, the adsorbent has no remaining active sites to be filled with the metal ions because of a comparable charge repulsion among the Pb(*II*) ion in dispersion and those already adsorbed by 3D adsorbent [29]. In this case, 3D printed control, PV/AA-B0, PV/AA-B20, and PV/AA-B25 constructs presented the quickest time of adsorption (*i.e.*, before adsorption equilibrium) of about 10, 9, 2, and 2 min, respectively. These results represented quicker adsorption kinetic mainly regarding 3D capsule-like objects with highly porous structures (Fig. 6). This finding also aligns with the previous NSR/NHF test (section 3.1.4), which indicated that the printed PV/AA-B20 and PV/AA-B25 structures exhibited the greatest NHF value. Following this initial quicker hydration, a concentration gradient of Pb (*II*) ions was created at the interface of gel–water, therefore starting diffusion of metal ions from the dispersion into 3D adsorbents. In this situation, the metal ions could instantly bind to the swollen polymeric structures [29]. In the plateau region, control, PV/AA-B0, PV/AA-B20, and PV/AA-B25 adsorbent offered an adsorption capacity of 382, 535, 694, and 896 mg g^{-1} respectively. Then, it is concluded that the presence of a sponge-like structure with a hierarchically macroporous architecture could improve the final adsorption capacity for Pb(*II*) ions.

Regarding adsorption capacity of 3D capsule-like adsorbents, *pseudo*-first-order (Eq. (9)) and *pseudo*-second-order (Eq. (10)) calculations were utilized to evaluate the regulatory mechanism of adsorption kinetics such as chemical reactions and mass transfer:

$$\log(q_e - q_t) = \log q_e - \frac{k_1}{2.303} t \tag{9}$$

$$\frac{t}{q_t} = \frac{1}{k_2 q_e^2} + \frac{t}{q_e} \tag{10}$$

Here, q_e and q_t (mg g^{-1}) specify the equilibrium adsorption capacity and adsorption capacity at time (t), respectively. The k_1 and k_2 are the rate constants of *pseudo*-first-order (1/min) and *pseudo*-second-order adsorption (g/mg min), respectively. To detect k_1 or k_2 constants, as well as the value of correlation coefficient (R^2), the log ($q_e - q_t$) or ($t\ qt^{-1}$)

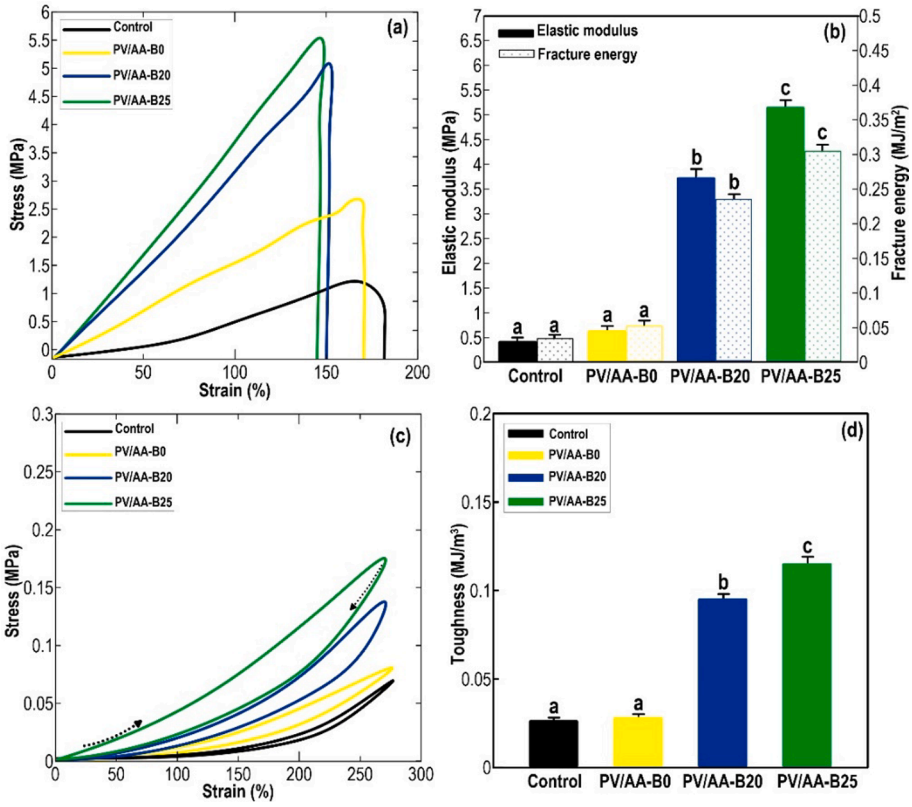

Fig. 7. Mechanical properties of different samples. (a) Stress–strain curve. (b) Elastic modulus and fracture energy bar diagrams. (c) Stress–strain curves after unloading–loading test at a 250% strain. (d) Toughness values bar diagram.

both as a function of t were plotted. The equation of $h = k_2 q_e^2$ was also utilized to measure the initial adsorption rate h (mg/g min) [29]. Table 3 lists the *pseudo*-first-order and *pseudo*-second-order calculations to evaluate the controlling mechanism concerning the adsorption process.

As Table 3 summarized, the levels of correlation coefficient concerning the kinetic plots of the *pseudo*-second-order equation were above 0.997 in comparison with the *pseudo*-first-order model, whose R^2 values were lower than 0.790. This obviously displays that the theoretical or experimental results are correlated well with the *pseudo*-second-order equation. According to our data, the adsorption process of 3D capsule-likes to remove Pb(*II*) ions could be controlled by physicochemical reactions [29]. Furthermore, compared to control and PV/AA-B0 samples, PV/AA-B20 and PV/AA-B25 adsorbents endowed a quicker adsorption rate with a greater ultimate adsorption capacity of Pb(*II*) ions. Specifically, these highly porous 3D structures with a mechanically tough structure were able to effectively eliminate the metal ions from wastewater.

3.3.2. Effect of pH

Since the acidity of the aqueous dispersions affects the physicochemical properties of pollutants and the functional groups on the adsorbent surface, the pH of the solution has a dominant role in the productivity of the adsorption process [29]. For this reason, different dispersion pHs (2–6) were examined to monitor the adsorption capacity of 3D printed capsule-like objects on the capture of Pb(*II*) ions (Fig. 8b). A rapid increase in the adsorption capacity of different 3D adsorbents was noted with increasing pH from 2.0 to 3.0, followed by a steady increase in the adsorption capacity. The dispersion pH has a great effect on the ion removal ability once water comprises an ionizable group due to an alteration in the ionization degree [29]. The ionizable groups are present in nonionized form mainly at a low pH. This inhibits their interaction with metal ions, where the adsorption capacity for Pb(*II*) was prominently decreased. With increasing pH, the ionizable groups can be ionized and improve their interaction with the metal ions in the aqueous dispersion, enhancing the adsorption capacity of Pb(*II*) ions [45]. By increasing the dispersion pH beyond 4, the H^+ concentration in the system principally was neglected regarding the level of Pb(*II*) ions. Thus, the adsorption capacity of 3D capsule-like objects on Pb(*II*) ions tended to be smooth as illustrated in Fig. 8b.

3.3.3. Adsorption isotherms for Pb(II)

The loading capacity of the adsorbent is also affected by the initial concentration of the adsorbate [29,45]. With increasing the initial concentration of Pb(*II*), the amount of adsorbed Pb(*II*) increased and continued almost constant by reaching the initial Pb(*II*) concentration about 600 mg/L (Fig. 8c) Compared to control and PV/AA-B0, PV/AA-B20 and PV/AA-B25 offered a greater adsorption capacity for Pb(*II*) at a lower initial Pb(*II*) concentration (<200 mg/L). To recognize the adsorption mechanism of 3D capsule-like objects on Pb(*II*), the adsorption result was created through different adsorption isotherm models, namely Freundlich and Langmuir adsorption isotherm equations. The Langmuir equation (Eq. (11) is based on the empirical equation of the structure of a homogeneous adsorbent, assuming the presence of a monolayer matrix, whereas the Freundlich model (Eq. (12) assumes that the adsorption process as multilayered adsorption occurs on a heterogeneous surface of an adsorbent. The two typical adsorption isotherm models are defined as follows:

$$\frac{c_e}{q_e} = \frac{1}{k_L q_m} + \frac{c_e}{q_m} \tag{11}$$

$$\ln(q_e) = \ln k_F + \frac{1}{n}\ln c_e \tag{12}$$

Here, c_e (mg g^{-1}) and q_e (mg g^{-1}) are adsorbate concentration in dispersion and ions adsorbed contents at equilibrium, respectively. The q_m (mg g^{-1}) denotes a capacity of monolayer adsorption for the

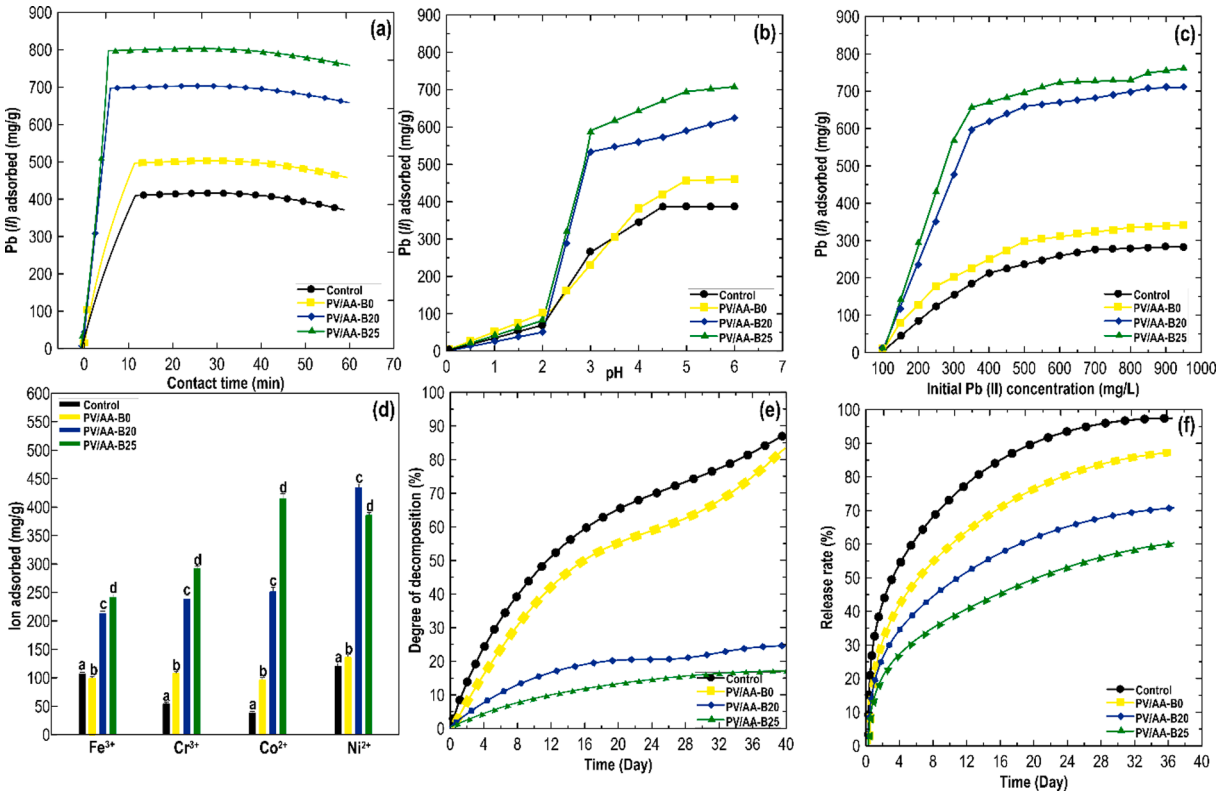

Fig. 8. Effects of (a) contact time, (b) pH of dispersion, (c) initial levels of Pb(*II*), and (d) different external interfering metal ions on Pb(*II*) adsorption capacity of 3D printed capsule-like adsorbents. All tests were conducted with the same reaction circumstance including Pb(*II*) ions with an initial level of 500 mg L^{-1}, mixing rate of 200 rpm, adsorbent weight of 25 mg, dispersion volume of 100 mL, and a temperature of 25 °C. (e) Stability comparison of solid K_2FeO_4 and printed capsule-like objects containing K_2FeO_4. (f) Effect of 3D adsorbent concentration on dinitro butyl-phenol (DNBP) removal (%). The experiment was performed with the same reaction circumstance including DNBP concentration = 40 mg L^{-1}; pH 6.5; reaction time = 80 min.

Table 3
The obtained *pseudo*-first-order and *pseudo*-second-order parameters regarding the adsorption capacity of each 3D capsule-like object for Pb(*II*).

Sample	*Pseudo*-first-order model				*Pseudo*-second-order model			
	q_e, exp (mg.g^{-1})	q_e, cal (mg.g^{-1})	k_1 (min^{-1})	R^2	q_e, exp (mg.g^{-1})	q_e, cal (mg.g^{-1})	k_2 (g.mg^{-1}.min^1)	R^2
Control	382	300	0.0198	0.756	382	368	0.0512	0.998
PV/AA-B0	535	391	0.0267	0.789	535	529	0.0502	0.997
PV/AA-B20	694	567	0.0312	0.751	694	684	0.0418	0.999
PV/AA-B25	896	688	0.0389	0.745	896	986	0.0250	0.999

adsorbent, K_L (mL g^{-1}) and K_F (mL g^{-1}) are the Langmuir and Freundlich constants, respectively, and n represents a heterogeneity factor. The C_e/q_e was plotted against C_e and ln (q_e) versus ln (C_e) obtained by the linear Langmuir and Freundlich curves to calculate the isotherm constants and correlation coefficients (R^2). Table 4 lists the adsorption isotherm parameters for Pb(*II*) adsorption, which shows that the highest adsorption capacity of Pb(*II*) ions by 3D printed adsorbents was sufficiently described by the Freundlich isotherm with a higher R^2. Thus, in the current work, the Freundlich isotherm was a suitable equation to describe the adsorption of Pb(*II*) ions. This suggests that the adsorption of Pb(*II*) ions could be multimolecular layer adsorption and occurred on a heterogeneous surface [29]. This result also verifies the prevailing sign of graft crosslinking copolymerization to enhance the adsorption capacity of 3D structures for Pb(*II*).

Table 4
Estimated adsorption isotherm parameters for Pb(*II*) adsorption in different 3D capsule-like objects.

Sample	**Langmuir model**			**Freundlich model**		
	q_m (mg g^{-1})	$K_L \times (10^{-3})$ (mL g^{-1})	R^2	K_F (mL g^{-1})	n^{-1}	R^2
Control	81	5.78	0.7030	0.017	0.83	0.9996
EB5	76	6.02	0.7245	0.016	0.88	0.9999
EB15	132	4.67	0.6756	0.010	0.67	0.9999
EB30	146	4.88	0.6988	0.005	0.35	0.9998

3.3.4. *Effect of foreign ions on adsorption*

Since wastewater always contains the endless amounts of different types of heavy metal ions, the role of extraneous interfering ions in the adsorption process should be assessed [29,44,45]. In the current study, the existence of other types of foreign metal ions such as iron(*III*) (Fe^{3+}), chromium(*III*) (Cr^{3+}), cobalt(*II*) (Co^{2+}), and Nickel(*II*) (Ni^{2+}) was studied to monitor the adsorption capacity of Pb(*II*) ions by 3D capsule-like objects. Fig. 8d shows the adsorption capacities of all 3D adsorbents for Pb(*II*) ions were markedly reduced owing to their adsorption interference by the foreign metal ions. In this case, the Pb(*II*) adsorption capacity of 3D adsorbents revealed a notable deviation because of the difference in the functionalities of each foreign ion. A possible chelation process and electrostatic association could befall in the extraneous

interfering ions and functional groups of 3D capsule-like objects, which magnitude of the chelation or electrostatic association may be not similar regarding every foreign metal ion [29]. Our investigation presented that 3D printed adsorbents only took up Pb(*II*) ions about half of their capacity owing to the adsorption interferences by foreign ions, which is likely due to the competition between Pb(*II*) and extraneous interfering ions in the adsorbent surface to entrap by the adsorbent. In contrast to Co^{2+} and Ni^{2+}, Fe^{3+} and Cr^{3+} ions were more simply adsorbed by 3D capsule-like objects because of their higher charge radius ratio, which resulted in a decreased Pb(*II*) adsorption capacity (Fig. 8d). Besides, it can be concluded that the metal ions adsorptions through these types of 3D adsorbents were not selective, therefore the 3D capsule-like objects are able to eliminate numerous non-organic pollutants from wastewater. As a whole, it is proposed that PV/AA-B20 and PV/AA-B25 offered greater metal ions adsorption capacity, representing faster adsorption kinetics with improved adsorption rate and final adsorption capacity.

The effectiveness of the 3D printed adsorbents as an adsorbent for heavy metal ions may be attributed to the combined impact of physical and chemical adsorption mechanisms, in which both PVA and grafted PAA are essential components in the adsorption procedure. The potential physicochemical processes in the adsorption of heavy metal ions by 3D printed objects (Scheme 1, Top) could be associated with the surface complexation and Lewis acid-base interactions between the heavy metal ions and hydroxyl functional groups found in the structure of the PVA or PAA matrices, with the assistance of the sharing of lone-pair electrons from oxygen atoms (Scheme 1, Bottom). Moreover, the adsorption of Pb (*II*) ions onto the surface of PVA and grafted PAA is also believed to occur through ion exchange and chelation between the positively charged Pb(*II*) and the nonionized/ionized carboxylic groups within the polymer chains of PVA and grafted PAA. This adsorption mechanism can be confirmed by observing the balance of adsorption provided by the pH change of the heavy metal aqueous dispersion. Hydrogels are three-dimensional cross-linked polymer networks that possess numerous functional groups capable of serving as adsorption sites through ion exchange and chelation. In an aqueous dispersion, –COOH groups of PVA and grafted PAA can be dissociated, resulting in the release of protons and a subsequent decrease in pH [69]. The pH level plays a crucial role in the adsorption of metal ions on polymer hydrogels. Previous study has investigated the impact of pH on the swelling behavior of hydrogels, revealing different behaviors as pH changes [70]. The swelling behavior of PVA and grafted PAA system at pH 4 aligns with the pKa value of vinyl alcohol and AA. When the pH value exceeds their pKa values, the carboxyl groups undergo a decomposition process, leading to the formation of carboxylate.

3.4. Stability and sustained release behavior of 3D printed capsule-like objects containing Fe(VI)

Ferrate(*VI*), an oxyanion FeO_4^{2-} with iron in the +6 oxidation state, is widely recognized as an environmentally friendly agent for water treatment. This is primarily due to its exceptional oxidizing potential, selectivity, and ability to form non-toxic final products, while minimizing the production of undesirable disinfection byproducts. In

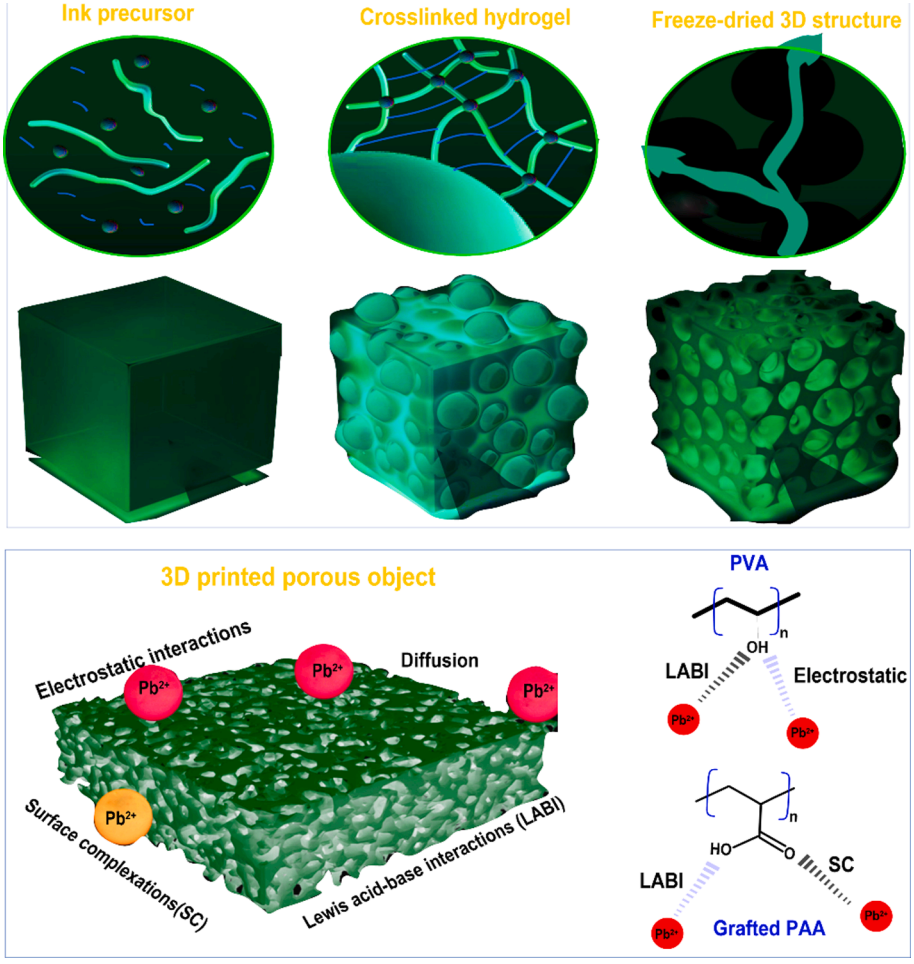

Scheme 1. Schematic presentation of (Top): Development of freeze-dried 3D objects and (Bottom): A possible physical and chemical adsorption mechanism of 3D printed objects for the adsorption of heavy metal ions.

advanced wastewater treatment, ferrate(*VI*) has demonstrated its capability to effectively remove micropollutants and precipitate phosphorus from biologically treated municipal wastewater. To assess the stability of the prepared printed capsule-like objects in air, a set of measurements was performed using different mass ratios of Fe(*VI*) to 3D capsule-like objects from 1:1 to 1:3, as well as pure K_2FeO_4. The experimental data showed that the decomposition degree of solid K_2FeO_4 in air increased more notably compared to Fe(*VI*)-contained capsule-like objects with the prolongation of conserved time. The decomposition degree of 3D structures including Fe(*VI*) with a mass ratio of 1:1, 1:2, and 1:3 (Fe(*VI*) to 3D constructs) in air were 14.8, 12.5, and 8.4 %, respectively, and the relating result concerning solid K_2FeO_4 was 91 % during 40 days. The considerably enhanced stability of Fe(*VI*)-capsulated 3D objects is likely related to the presence of wall materials, which could entrap the solid K_2FeO_4, protecting it from water and decreasing substances in the environment.

The sustained release behavior of the capsule-like objects in 8.0 M KOH solution at 25 °C is shown in Fig. 8e. It was revealed that the release rate of K_2FeO_4 from 3D objects with a mass ratio of 1:1, 1:2, and 1:3 (Fe(*VI*) to capsule-like objects) reached 90.4, 73.6, and 44.1 %, respectively, at the first region of plot, and 97.4, 88.8, and 69.1 %, respectively, at the end of plot. The data presented that the highly porous printed capsule-like objects with a greater mass ratio included more wall materials and had a thicker film around their core material so that the Fe(*VI*) was more slowly released.

To investigate the release kinetics of the K_2FeO_4 from the printed porous capsule-like objects, the kinetic constant k was performed by calculating their various mass levels. Data obtained from the controlled release tests were tested graphically for fitting various kinetic equations including the zero-order kinetic equation, the first-order kinetic model, the Higuchi equation [71], and the Ritger–Peppas equation [72]. In the current study, the Ritger–Peppas model was selected due to the best fit for the Fe(*VI*)-capsulated 3D objects, where the fractional Fe(*VI*) release Q changing with time t, which can be measured as follows:

$$Q = kt^n \tag{13}$$

Here, Q is the fractional Fe(*VI*) release, k is a kinetic constant, t is the release time and n is the diffusional exponent.

The Ritger–Peppas model predicts a linear curve between ln (Q) and ln (t) values, where kinetic constant (k) and diffusional exponent (n) were measured through the ordinate axis intercept and the slope of the straight line, respectively. Table 5 summarizes the predicted n and k values for the printed Fe(*VI*)-contained capsule-like object with different mass ratios. It also can be seen that the Fe(*VI*) releasing process regarding the prepared capsule-like object in 8.0 M KOH solution was associated with the Ritger–Peppas model, in which the releasing mechanism is non-Fick's diffusion. The results also showed that with increasing mass ratios of 3D object the kinetic constant k reduced.

3.5. Application of Fe(VI)-contained capsule-like objects in real wastewater treatment

In the treatment of dissolved contaminants in groundwater, encapsulation, and control-release technology have proven to be highly efficient methods. Encapsulation enables the slow and controlled release of Fe(*VI*). As a multifunction chemical reagent, the utilization of printed Fe(*VI*)-contained capsule-like objects can endow a notable compensation with regards to improving the ferrate(*VI*) salts stability with a more effective and inexpensive method. This can be considered an efficient practical value for wastewater treatment on the whole. An operational evaluation was conducted to measure the potential application of printed Fe(*VI*)-contained capsule-like objects for chemical oxygen demand (*COD*) and decolorization decrease (data not shown) of wastewater from dinitro butyl-phenol (DNBP) manufacturing. The unique orange color wastewater regarding this assessment was offered by Tairui Fine Chemical Co., Ltd.. The *COD* and the color of the samples were estimated by the dichromate method and the Platinum–Cobalt Standard method, respectively [73]. To accomplish the elimination of color and reduction in *COD*, the test was performed through the real wastewater with 1.0 g/L printed Fe(*VI*)-contained capsule-like objects at pH 6 with 80 min reaction time. The decrease in color and removal of *COD* regarding the wastewater treatment were detected to be 91 % and 73 %, respectively, confirming the demolition of the organic pollutants from wastewater. The printed capsule-like object was not readily degraded by Fe(*VI*) under the reaction conditions and was separated from the experiment dispersion simply by a modest filtration operation. As the industrial wastewater including the one studied in the current work comprises a complex combination of chemical compounds, the printed Fe(*VI*)-contained capsule-like object can be promising to serve as a full-scale wastewater treatment including numerous industrial effluents and harmful organic pollutants.

Table 5
The calculated values of diffusional exponent (n) and kinetic constant (k) for the capsule-like objects with different mass ratios of Fe(*VI*) to 3D object.

Different mass ratios of Fe(*VI*)-contained capsule-likes	n	k	R^2
1:1	0.311	24.12	0.9843
1:2	0.398	15.02	0.9911
1:3	0.361	10.78	0.9858

4. Conclusion

A hydrogel printable ink based on poly(vinyl alcohol)/acrylic acid was successfully crosslinked by UV irradiation/Norrish type *II* photosensitizer and after that it was 3D printed through an extrusion-type printing system to produce 3D capsule-like objects with a high level of porosity. The rheological, thermal, and structural characteristics showed the development of the inter- or intramolecular crosslinking linkages in the printing hydrogels, creating the mechanically robust printed capsule-like objects. After printing, the mechanical feature of 3D capsule-like objects treated with a higher content of photosensitizer showed higher tensile strength and toughness compared to that of crosslinked by a lower content. The crosslinked capsule-like objects endowed the enhancement in viscoelasticity and shear-thinning behavior, developing a structured 3D printed construct. Moreover, a hierarchically porous capsule-like objects with a high degree of specific surface area was engineered, meeting a prerequisite for potential application in water purification. A Freundlich isothermal equation well fitted to the experimental adsorption outcome, offering a highest adsorption capacity of Pb(*II*) ions using 3D objects. The prepared printed capsule-like objects containing Fe(*VI*) were also detected to be effectual in decolorizing and *COD* decreasing from real wastewater, which endowed the utilization of printed Fe(*VI*)-contained capsule-like objects to degrade several organic pollutants and industrial effluents more practical. Accordingly, 3D capsule-like objects effectually serve as a 3D printed adsorbent, which rapidly entraps inorganic pollutants instantly with maximum adsorption capacity, which can be favorable in additive manufacturing of biomaterials used for real water purification.

Author contributions

The manuscript was written through the contributions of all authors. All authors have approved the final version of the manuscript.

Funding

The research funding was provided by the University of Natural Resources and Life Sciences Vienna (BOKU).

CRediT authorship contribution statement

Peyman Asghartabar Kashi: Methodology, Investigation, Data curation, Formal analysis, Writing – original draft. **Adeleh Mohammadi:** Methodology, Investigation, Data curation. **Jianshe Chen:** Writing – review & editing, Validation, Methodology. **Rammile Ettelaie:** Writing – review & editing, Validation, Conceptualization. **Henry Jäger:** Writing – review & editing, Validation, Conceptualization. **Mahdiyar Shahbazi:** Writing – review & editing, Writing – original draft, Visualization, Validation, Supervision, Software, Resources, Project administration, Methodology, Investigation, Funding acquisition, Formal analysis, Data curation, Conceptualization.

Declaration of competing interest

The authors declare that they have no known competing financial interests or personal relationships that could have appeared to influence the work reported in this paper.

Data availability

Data will be made available on request.

Appendix A. Supplementary data

Supplementary data to this article can be found online at https://doi.org/10.1016/j.seppur.2024.127247.

References

[1] J.F. Pesqueira, M.F.R. Pereira, A.M.J. Silva, Clean. Prod. 261 (2020) 121078.
[2] L. Rizzo, W. Gernjak, P. Krzeminski, S. Malato, C.S. McArdell, J.A.S. Perez, H. Schaar, D. Fatta-Kassinos, Sci. Total Environ. 710 (2020) 136312.
[3] T. Pointet, LHB 108 (1) (2022) 2090867.
[4] P. Krzeminski, M.C. Tomei, P. Karaolia, A. Langenhoff, C.M.R. Almeida, E. Felis, F. Gritten, H. Rasmus Andersen, T. Fernandes, C.M. Manaia, L. Rizzo, D. Fatta-Kassinos, Sci. Total Environ. 648 (2019) 1052–1081.
[5] R.K. Yadav, S. Das, S.A. Patil, Trends Biotechnol. 41 (4) (2023) 484–496.
[6] B.S. Rathi, P.S. Kumar, P.L. Show, J. Hazard. Mater. 409 (2021) 124413.
[7] R.P. Schwarzenbach, B.I. Escher, K. Fenner, T.B. Hofstetter, C.A. Johnson, U. Von Gunten, B. Wehrli, Science 313 (5790) (2006) 1072–1077.
[8] F. Fu, Q. Wang, J. Environ. Manage. 92 (3) (2011) 407–418.
[9] P.A. Alaba, N.A. Oladoja, Y.M. Sani, O.B. Ayodele, I.Y. Mohammed, S.F. Olupinla, W.M.W. Daud, J. Environ. Chem. Eng. 6 (2) (2018) 1651–1672.
[10] M. Shahbazi, H. Jäger, R. Ettelaie, J. Chen, A. Mohammadi, P.A. Kashi, Addit. Manuf. 81 (2023) 103977.
[11] L.H. Chen, M.H. Sun, Z. Wang, W. Yang, Z. Xie, B.L. Su, Chem. Rev. 120 (20) (2020) 11194–11294.
[12] Q. Gu, T.C.A. Ng, Y. Bao, H.Y. Ng, S.C. Tan, J. Wang, J. Chem. Eng. 428 (2022) 130456.
[13] G. Franchin, J. Pesonen, T. Luukkonen, C. Bai, P. Scanferla, R.S. Botti, Carturan, M. Innocentini, P. Colombo, Mater. Des. 195 (2020) 109006.
[14] L. Li, Q. Li, Y. Feng, K. Chen, J. Zhang, A.C.S. Appl, Mater, Interfaces 14 (1) (2021) 2360–2368.
[15] S. Ma, H. Yang, S. Fu, P. He, X. Duan, Z. Yang, D. Jia, P. Colombo, Y. Zhou, J. Hazard. Mater. 443 (2023) 130161.
[16] L. Long, R. Pei, Y. Liu, X. Rao, Y. Wang, S.F. Zhou, G.J. Zhan, Hazard. Mater. 423 (2022) 126983.
[17] S. Lawson, M. Snarzyk, D. Hanify, A.A. Rownaghi, F. Rezaei, Ind. Eng. Chem. Res. 59 (15) (2019) 7151–7160.
[18] Z. Liu, X. Xia, W. Li, L. Xiao, X. Sun, F. Luo, Q. Chen, Q. Qian, Materials 13 (19) (2020) 4403.
[19] M. Shahbazi, H. Jäger, A.C.S. Appl, Bio Mater 4 (1) (2020) 325–369.
[20] M. Shahbazi, H. Jäger, R. Ettelaie, A.C.S. Appl, Mater, Interfaces 14 (18) (2022) 21392–21405.
[21] M. Shahbazi, H. Jäger, R. Ettelaie, A. Mohammadi, P.A. Kashi, Addit. Manuf. 71 (2023) 103598.
[22] H. Ding, S. Barg, B. Derby, Nanoscale 12 (21) (2020) 11440–11447.
[23] M. Shahbazi, H. Jäger, R. Ettelaie, Biomacromolecules 22 (11) (2021) 4592–4605.
[24] M. Shahbazi, H. Jäger, A. Mohammadi, P.A. Kashi, J. Chen, R. Ettelaie, ACS Appl. Mater. Interfaces 15 (42) (2023) 49874–49891.
[25] W.S. Tan, C.K. Chua, T.H. Chong, A.G. Fane, A. Jia, Virtual Phys. Prototyp. 11 (3) (2016) 151–158.
[26] M. Shahbazi, H. Jäger, R. Ettelaie, Addit. Manuf. 57 (2022) 102934.
[27] G. Zhou, K.P. Wang, H.W. Liu, L. Wang, X.F. Xiao, D.D. Dou, Y.B. Fan, Int. J. Biol. Macromol. 113 (2018) 792–803.
[28] M. Peydayesh, R. Mezzenga, Nat. Commun. 12 (1) (2021) 3248.
[29] M. Shahbazi, H. Jäger, S.J. Ahmadi, M. Lacroix, Carbohydr. Polym. 240 (2020) 116211.
[30] D.Q. Cao, X. Song, X.M. Fang, W.Y. Yang, X.D. Hao, E. Iritani, N. Katagiri, J. Chem. Eng. 354 (2018) 866–874.
[31] J.M. Yang, H.Z. Wang, C.C. Yang, J. Membr. Sci. 322 (1) (2008) 74–80.
[32] M. Shahbazi, H. Jäger, R. Ettelaie, M. Ulbrich, Biomacromolecules 24 (1) (2021) 69–85.
[33] Y. Zhang, L. Zhang, R. Gao, L. Zhong, J. Xue, Carbohydr. Polym. 267 (2021) 118227.
[34] F.C. do Nascimento, L.C.V. de Aguiar, L.A.T. Costa, M.T. Fernandes, R.J. Marassi, A.D.S. Gomes, J.A. de Castro, Polym. Bull. 78 (2) (2021) 917–929.
[35] L. Chen, J. Dai, B. Hu, J. Wang, Y. Wu, J. Dai, M. Meng, C. Li, Y. Yan, Sep. Purif. Rev. 49 (4) (2020) 265–293.
[36] C. Decker, K. Zahouily, J. Polym. Sci. A Polym. Chem. 36 (14) (1998) 2571–2580.
[37] J.P. Deng, W.T. Yang, B. Rånby, J. Appl. Polym. Sci. 77 (7) (2000) 1513–1521.
[38] T. Kondo, M. Koyama, H. Kubota, R. Katakai, J. Appl. Polym. Sci. 67 (12) (1998) 2057–2064.
[39] D. Ruckert, G. Geuskens, Eur. Polym. J. 32 (2) (1996) 201–208.
[40] M. Shahbazi, S.J. Ahmadi, A. Seif, G. Rajabzadeh, Food Hydrocoll. 61 (2016) 378–389.
[41] W.T. Yang, B. Rånby, Polym. Bull. 37 (1996) 89–96.
[42] S.G. Xu, Y.F. Sun, J.M. Du, W.T. Yang, J. Beijing Univ. Chem. Technol. 27 (4) (2000) 29.
[43] R.H. Ewoldt, P. Winter, J. Maxey, G.H. McKinley, Rheol. Acta 49 (2010) 191–212.
[44] Y. Zheng, A. Wang, J. Hazard. Mater. 171 (1–3) (2009) 671–677.
[45] J. Maity, S.K. Ray, Carbohydr. Polym. (2018,182,) 159–171.
[46] E. Andrzejewska, Prog. Polym. Sci. 26 (4) (2001) 605–665.
[47] M. Chen, M. Zhong, J.A. Johnson, Chem. Rev. 116 (17) (2016) 10167–10211.
[48] S. Villarruel, L. Giannuzzi, S. Rivero, A. Pinotti, Mater. Sci. Eng. C 56 (2015) 545–554.
[49] Y. Zhang, P.C. Zhu, D. Edgren, J. Polym. Res. 17 (2010) 725–730.
[50] M. Shahbazi, G. Rajabzadeh, A. Rafe, R. Ettelaie, S.J. Ahmadi, Food Hydrocoll. 71 (2017) 259–269.
[51] X. Zhang, K. Takegoshi, K. Hikichi, Polym. J. 23 (2) (1991) 79–86.
[52] Z. Tang, J. Wei, L. Yung, B. Ji, H. Ma, C. Qiu, K. Yoon, F. Wan, D. Fang, B.S. Hsiao, B. Chu, J. Membr. Sci. 328 (1–2) (2009) 1–5.
[53] E. Makhado, S. Pandey, P.N. Nomngongo, J. Ramontja, Carbohydr. Polym. 176 (2017) 315–326.
[54] X. Wei, H. Tao, C. Tan, J. Xie, F. Yuan, L. Guo, B. Cui, F. Zou, W. Gao, P. Liu, L. Lu, Int. J. Biol. Macromol. 239 (2023) 124211.
[55] A. Hasimi, A. Stavropoulou, K.G. Papadokostaki, M. Sanopoulou, Eur. Polym. J. 44 (12) (2008) 4098–4107.
[56] Y. Nishio, R.J. Manley, Macromolecules 21 (5) (1988) 1270–1277.
[57] M. Krumova, D. Lopez, R. Benavente, C. Mijangos, J.M. Perena, Polymer 41 (26) (2000) 9265–9272.
[58] H. Adelnia, R. Ensandoost, S.S. Moonshi, J.N. Gavgani, E.I. Vasafi, H.T. Ta, Eur. Polym. J. 164 (2022) 110974.
[59] E. C. Bingham, (1917) No. 278.
[60] H.A. Barnes, J. Nonnewton, Fluid Mech. 81 (1–2) (1999) 133–178.
[61] T. Osswald, N. Rudolph, **2015**, *Carl Hanser, München.*
[62] C.W. Macosko, Measurements and Applications (1994).
[63] A. Malkin, V. Kulichikhin, S. Ilyin, Rheol. Acta 56 (2017) 177–188.
[64] K. Hyun, M. Wilhelm, C.O. Klein, K.S. Cho, J.G. Nam, K.H. Ahn, S.J. Lee, R. H. Ewoldt, G.H. McKinley, Prog. Polym. Sci. 36 (12) (2011) 1697–1753.
[65] T. Voigtmann, Curr. Opin. Colloid Interface Sci. 19 (6) (2014) 549–560.
[66] M. Shahbazi, H. Jäger, R. Ettelaie, J. Chen, A. Mohammadi, P.A. Kashi, M. Ulbrich, Curr. Res. Food Sci. 8 (2024) 100686.
[67] H.A. Balogun, R. Sulaiman, S.S. Marzouk, A. Giwa, S.W. Hasan, J. Water Process Eng. 31 (2019) 100786.
[68] A.T. Paulino, L.A. Belfiore, L.T. Kubota, E.C. Muniz, V.C. Almeida, E.B. Tambourgi, Desalination 275 (1–3) (2011) 187–196.
[69] Y. Zheng, S. Hua, A. Wang, Desalination 263 (1–3) (2010) 170–175.
[70] Z. Lin, Y. Hu, Y. Yuan, B. Hu, B. Wang, Ecotoxicol. Environ. Saf. 208 (2021) 111451.
[71] T.J.J.O.P.S. Higuchi, Mechanism of sustained-action medication. Theoretical analysis of rate of release of solid drugs dispersed in solid matrices, J. Pharm. Sci. 52 (12) (1963) 1145–1149.
[72] P.L. Ritger, N.A. Peppas, A simple equation for description of solute release I. Fickian and non-fickian release from non-swellable devices in the form of slabs, spheres, cylinders or discs, J. Control. Release 5 (1) (1987) 23–36.
[73] H. Wang, H.L. Wang, W.F. Jiang, Z.Q. Li, Photocatalytic degradation of 2, 4-dinitrophenol (DNP) by multi-walled carbon nanotubes (MWCNTs)/TiO2 composite in aqueous solution under solar irradiation, Water Res. 43 (1) (2009) 204–210.